“Dynamic growth re-orientation orchestrates flatness in the Arabidopsis leaf”

Kate Harline[1,2], Antoine Fruleux[3], Brendan Lane[4], Gabriella Mosca[5], Soeren Strauss[6], Nik Tavakolian[7], James W. Satterlee[2], Chun-Biu Li[7], Abhyudai Singh[8], Richard S. Smith[4], Arezki Boudaoud[9], Adrienne H.K. Roeder[1,2]

[1]Weill Institute for Cell and Molecular Biology, Cornell University, Ithaca, NY 14853, USA
[2]Section of Plant Biology, School of Integrative Plant Sciences, Cornell University, Ithaca, NY 14853, USA
[3]LPTMS, CNRS, Université Paris-Saclay, 91405, Orsay, France.
[4]John Innes Centre, Norwich Research Park, Norwich, NR4 7UH, UK
[5]Department of Physics, Technical University of Munich, 85748 Garching b. München, Germany
[6]Department of Comparative Development and Genetics, Max Planck Institute for Plant Breeding Research, Carl von Linne Weg 10, 50829 Cologne, Germany
[7]Department of Mathematics, Stockholm University, Stockholm 10691, Sweden
[8]Department of Electrical and Computer Engineering, Biomedical Engineering, University of Delaware, Newark, Delaware 19716
[9]LadHyX, CNRS, Ecole Polytechnique, IP Paris, 91128 Palaiseau Cedex, France

Running title: Leaves flatten by re-orienting growth

*Author for correspondence: ahr75@cornell.edu

Abstract

The growth and division of cells in plant leaves is highly dynamic in time and space, all while the cells cannot move relative to their neighbors. Given these constraints, models predict that long range regulatory systems must exist to maintain flat forms. Juxtaposed microRNA (miRNA) networks could serve as one of these regulatory systems. One of these miRNAs, miR319 is thought to be expressed from the base of leaves and to promote growth by degrading class II TCP transcription factor mRNAs. A miR319 overexpression mutant, *jagged and wavy (jaw-D)* exhibits rippling and undulating leaves, consistent with biomechanical predictions that without genetic spatial coordination, tissues will deform. It has been theorized that *jaw-D* rippling results from overgrowth at the margins, however this does not fully address how miR319 expression from the base of wild-type (WT) leaves allows them to flatten. Here, we track the growth, cell division and cell maturation in live WT and *jaw-D* leaves to ask how miR319 expression in WT promotes flattening. This data revealed the importance of spatially distinct growth, division and differentiation patterns in WT leaves, which are missing in *jaw-D*. We propose that WT leaf cells respond to differentiation cues to dynamically re-orient growth in specific tissue locations and regulate flattening.

Introduction

In nature, leaves exhibit a myriad of shapes and sizes. Yet, all leaves initially begin as a few cells recruited from the shoot apical meristem (SAM) (Rodriguez et al., 2014; Sarojam et al., 2010; Reinhardt et al., 2003; Caggiano et al., 2017; Nakata et al., 2012). Understanding how these few initial cells create recognizable forms in nature requires a rich combination of biophysical principles and genetic pathways. Imaging at multiple scales has revealed that development and growth in leaves is highly spatially and temporally dynamic (Armon et al., 2021; Avery, 1933; Kuchen et al., 2012; Fox et al., 2018; Derr et al., 2018; Poethig and Sussex, 1985). In most species, leaf organs exhibit a dynamic progression from fast to slow growth with a gradient of slow growth initiating from the tip and progressing downward. The slowing of growth from the tip corresponds with a wave of cellular differentiation that initiates at the tip (Avery, 1933; Remmler and Rolland-Lagan, 2012; Das Gupta and Nath, 2015; Poethig and Sussex, 1985). Biomechanical principles predict that juxtaposition of different growth rates within a tissue would result in tissue

deformations including leaf curling and ruffling (Boudaoud, 2010; Hamant et al., 2008; Sharon et al., 2002; Marder et al., 2003). Further, the juxtaposition of different growth rates has been posited as a mechanism to fold and shape floral organs (Rebocho et al., 2017). Yet leaves are usually flat, which is optimal for their physiological functions of photosynthesis and gas exchange. To obtain their flat form, leaves must be able to coordinate their growth at large spatial scales (Marder et al., 2003).

A few signals have been proposed to function along the leaf length to guide leaf differentiation and coordinate growth in flat leaves (Kazama et al., 2010; Sauret-Güeto et al., 2013). Pertinent to this study are a pair of microRNAs (miRNAs), miR319 and miR396, with complementary spatial patterns. miRNAs have been proposed to act as mobile signals to guide organ-level processes (Skopelitis et al., 2012). Members of the miR319 family have shown promoter expression at the base of leaves (miR319c) and floral organs (miR319a, c) (Challa et al., 2019; Nag et al., 2009). miR319 targets the class II *TEOSINTE BRANCHED 1, CYCLOIDEA, PROLIFERATING CELL NUCLEAR ANTIGEN FACTOR 1 AND 2 (TCP)* transcription factors which have been shown to repress growth and activate tissue differentiation (Schommer et al., 2008; Efroni et al., 2008; Bresso et al., 2018; Sarvepalli and Nath, 2011). miR319 targets, especially *TCP4* are thought to regulate cell growth and differentiation through *CUP-SHAPED COTYLEDONS 2 (CUC2)* and the *CUC* regulator miR164 as well as auxin and cytokinin networks (Rubio-Somoza et al., 2014; Koyama et al., 2017, 2010; Challa et al., 2019, 2021).

Complementarily, miR396 is expressed from the tips of growing leaves and targets the *GROWTH-REGULATING FACTOR (GRF)* family of transcription factors for degradation (Debernardi et al., 2012, 2014). This likely creates a gradient of *GRF* with a maximum at the base of leaves (Rodriguez et al., 2010). *GRFs* promote growth and their overexpression can lead to overall increases in leaf size, though not curling (Beltramino et al., 2018). miR396 has also been shown to repress expansion promoted by the *GRFs* in roots, where miR396 exclusion of *GRFs* seems important for maintaining the meristematic nature of transit-amplifying cells (Rodriguez et al., 2015). There is a direct interaction between TCP4 and the regulatory sequence of miR396 so crosstalk between these contrasting pathways is likely (Schommer et al., 2014). Taken togeth-

er, this suggests that the restriction of *GRF* expression to the base by miR396 and restriction of *TCP*s to the tip by miR319 could establish the characteristic leaf growth gradient, but does not clarify how this juxtaposition of fast and slow growth is resolved by the leaf to flatten (Avery, 1933; Remmler and Rolland-Lagan, 2012).

miR319 was discovered in an activation tagging screen, where the mutant, named *jagged and wavy (jaw-D)* was found to overexpress the miR319 hairpin locus (Palatnik et al., 2003; Weigel et al., 2000). *jaw-D* exhibits curly and wavy leaves. This curling has previously been attributed to extended growth from an over-active marginal meristem, although these studies have relied on cell cycle reporters as a proxy for assessing tissue material addition (Avery, 1933; Alvarez et al., 2016). Tissue augmentation involves both cell divisions and growth by expansion, processes with distinct regulation and developmental timing (Traas and Doonan, 2001). Serrations and lobing – distinct from the curling and rippling in *jaw-D* – have also more directly been attributed to differential growth repression and activation along the margin (Zhang et al., 2020; Blein et al., 2013; Kierzkowski et al., 2019; Chuck et al., 1996). However, the presence and importance of a marginal meristem in shaping leaves has long been equivocal (Donnelly et al., 1999). Further, it remains to be established how WT expression of miR319, graded along the proximal-distal axis, would laterally guide the formation of simple margins and flat leaves. Biomechanical models predict wavy deformations will occur where spatial coordination of heterogeneous leaf growth is absent (Armon et al., 2021; Marder et al., 2003). We wondered if we could link disruptions in the genetic regulatory capacity in *jaw-D* with faulty growth heterogeneity regulation and thus infer how WT leaves flatten properly.

The regulation of TCPs by miR319 is well-conserved within angiosperms (Warthmann et al., 2008; Palatnik et al., 2007). Therefore, the insights gained from studies of this pathway could have broad implications for the flattening of leaves throughout the angiosperms. Notable homologs in other model species include the class II- defining member *CINCINNATA (CIN)* in snapdragon and *Lanceolate* in tomato (Nath et al., 2003; Crawford et al., 2004; Ori et al., 2007), both of which when mutated or downregulated yield rippling and undulating leaves like the miR319 overexpression mutant *jaw-D.* Increased curvature in *cin* leaves was attributed to decreased per-

ception of a tip-derived differentiation signal and thus an escape from leaf margin growth regulation (Nath et al., 2003). Still, the connection between a proximal-distal differentiation signal and marginal growth remains to be resolved.

To understand how leaf shape emerges from and reconciles spatially distinct cellular growth, divisions and differentiation, we have tracked the growth, cell division and cell maturation in real time in living wild type and *jaw-D* mutant leaves. Because *jaw-D* overexpresses miR319, we expected to see an expansion of growth and delay in tissue maturation corresponding with expanded miR319 presence. Only our tissue maturation hypothesis proved correct. Growth and cell division were spread more distally in *jaw-D,* but had a lower maximum value than WT. Our live imaging results allowed us to explore the relationship between growth rate, growth orientation, and differentiation. Based on our results, we propose that *jaw-D* leaves fail to dynamically re-orient growth leading to growth conflicts and resulting in increased curvature. Our data suggests that a distal differentiation signal, that cannot be perceived in *jaw-D* may be required to induce growth re-orientation in WT. Thus, we help resolve how a proximal-distally oriented signaling network can orchestrate leaf flattening medio-laterally.

Results

Features of leaf form emerge soon after primordia initiation

To understand how the three dimensional form of the leaf arises from cellular growth patterns, we repeatedly imaged living wild-type (WT) and *jaw-D* mutant first leaves from 3 days after sowing (DAS) to 8 or 9 DAS (n = 3 leaves for each genotype; Figure 1A). Cell boundaries were marked with a fluorescent plasma membrane marker. To increase the surface of the leaf that could be imaged, the cotyledons were dissected off. We used confocal microscopy to image nearly the entire abaxial (bottom) epidermis of the leaf at cellular resolution so that we could make cellular and organ scale measurements. Then we used MorphoGraphX 2.0 image analysis software to represent the confocal stacks as 2.5D curved mesh surfaces (Strauss et al., 2022). We segmented the epidermal cell signal projected on this mesh and tracked each of the cellular lineages over time.

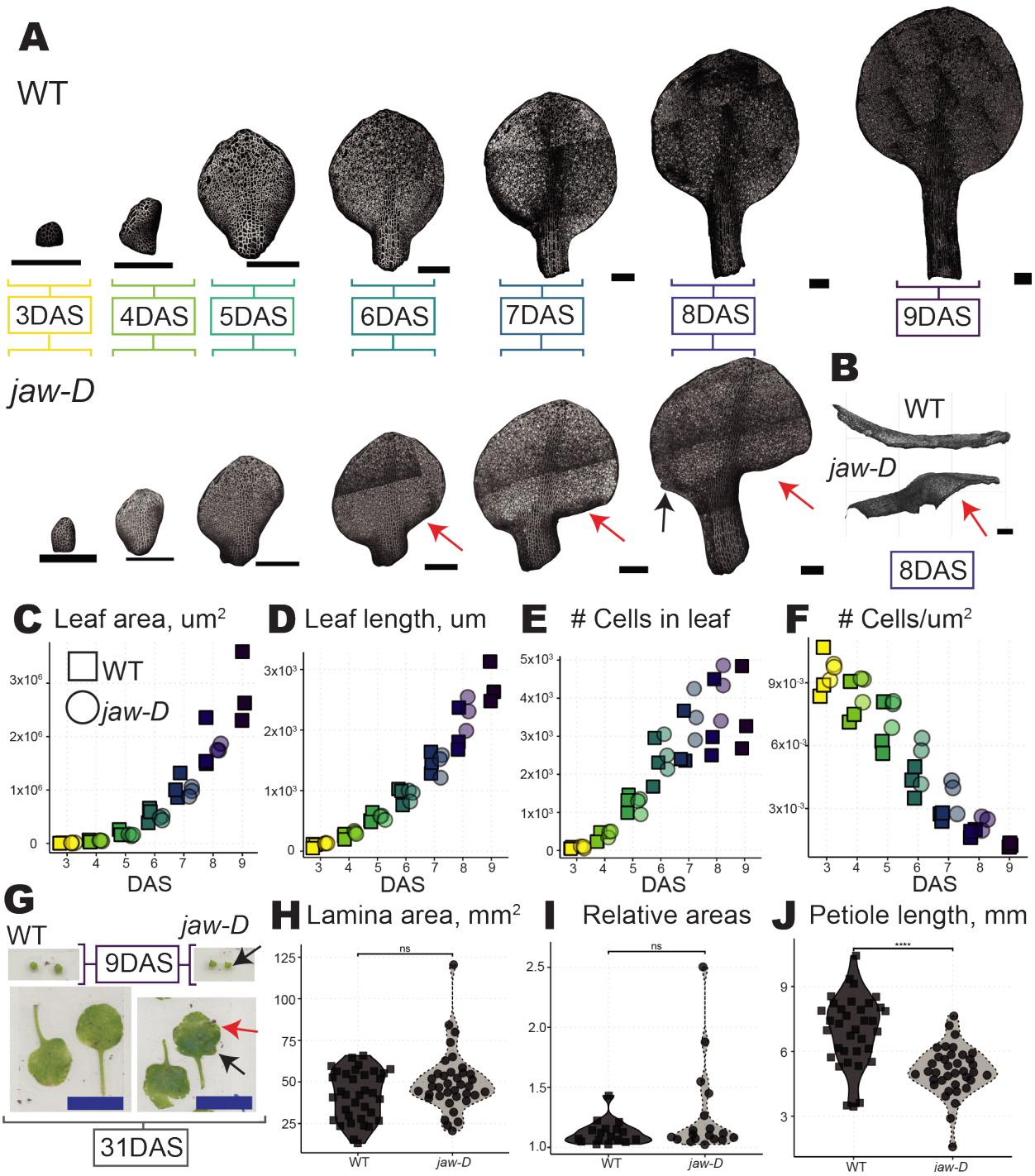

Figure 1. | Features of leaf form emerge soon after primordia initiation (A) Signal from confocal stacks of WT (top) and *jaw-D* (bottom) leaves from 3 DAS to 9 DAS are shown projected onto 2.5D surface meshes rendered in MorphoGraphX 2.0. Tissue differentiation in WT and its disruption in *jaw-D* can be seen starting at 5 DAS. (A, G) Black arrows indicate the beginnings of leaf dimples and red arrows indicate increased curvature in early *jaw-D* leaves that will be-

In all samples we observed rapid cellular and organ-wide morphology changes characteristic of early leaf growth (Figure 1A, Supplemental Figures 10-15). Notably, at 4 DAS stomata begin to initiate at the distal end of the leaf and at 5 DAS a cylindrical fold in the proximal base of the leaf begins to differentiate the petiole (stalk that attaches the leaf to the stem) from the lamina (the flat leaf surface) in WT and *jaw-D* leaves. While at 5 DAS pavement cells in WT leaves begin initiating their characteristic puzzle shape, *jaw-D* leaves produce more modest lobing. Note, while the *jaw-D* sample leaf may appear left-right asymmetric, this is an artifact of viewing the mesh in two dimensions due to the position it was imaged in and, other samples have positions

---

come ripples at maturity. (A-B,G) Black scale bars = 200 µm. (B) Side view of 8 DAS leaf meshes, with petiole on the left and tip on the right, show a global increase in leaf curvature in *jaw-D* (lower) versus WT (upper). (C) Total segmented leaf area and (D) length increase exponentially over the course of the live imaging experiment in WT and *jaw-D* plants. (E) The number of segmented cells in WT and *jaw-D* begins to plateau around 6 DAS, suggesting that the major phase of cell division is ending. (F) Cell density determined as the number of cells per area segmented. The density is mostly linear from 3-7 DAS in *jaw-D* and WT but begins to show asymptotic behavior reflective of plateauing cell numbers. (C-F) Squares indicate WT leaves, circles indicate *jaw-D* leaves. Colors indicate DAS. Means for all measures for each time point were not significantly different (paired Student's t-tests with Bonferroni correction). (A-F) n=3 leaves for each genotype. (G) Comparison of dimensions in the first and second leaves of WT (left) and *jaw-D* (right) at the final point in WT imaging, 9 DAS (top) and mature leaves, at least 31 DAS (bottom). Blue scale bars indicate 10 mm. (H) Final lamina area for the first and second leaves of WT and *jaw-D*. WT leaf areas exhibit a broad and bimodal distribution, whereas *jaw-D* leaf areas center tightly around the median with more extreme values ($p > 0.05$, Wilcox test). (H-J) Color, shape and linetype indicate genotype (solid, dark gray, squares = WT, dotted, light gray, circles = *jaw-D*) (I) Relative area between the final sizes of the first and second leaves of the same plant in WT or *jaw-D*. *Jaw-D* first and second leaves on the same plant have a greater spread of values and more extreme values (Feltz and Miller asymptotic test of CV $p = 3.051466e-05$). (J) Length of petioles in fully grown first and second leaves of WT and *jaw-D*. *jaw-D* petioles are shorter ($p < .0001$, Wilcox test).

that lack this visual skew (Supplemental Figure 12). Organ-wide morphological features of the 3-8 DAS leaves, including length, area, cell number and cell density, were not statistically different between WT and *jaw-D* (paired Student's t-tests with Bonferroni correction, Figure 1C-F). Therefore, we concluded that WT and *jaw-D* leaves could be considered at the same stage for each day in the experiment. However, the enhanced curvature of *jaw-D* prevented cell segmentation in some of the proximal regions, so it is likely that proximal *jaw-D* cells are undercounted. While leaf area and leaf length continued to increase exponentially throughout the experiment (log(leaf area) ~ time, $R^2 = 0.93$, $p < 2.2e-16$; log(leaf length) ~ time, $R^2 = 0.94$, $p < 2.2e-16$, Supplemental Figure 1F-G), cell number began to plateau (three parameter log-logistic Lack of fit p-value = 0.95) around 6 DAS, suggesting that we captured the transition of leaves from growth associated with cell division to growth predominately through cell expansion (Figure 1E) (Rodriguez et al., 2014). Additionally, the density, the number of cells per area, stayed mostly linear, but was approaching a negative exponential curve in the last two time points in WT, suggestive of a more complete transition to expansion-based growth in WT (cell density ~ time, $R^2 = 0.92$, $p < 2.2204e-16$).

To relate the phenotypes we captured early in leaf development to phenotypes of fully developed leaves, we scanned WT and *jaw-D* leaves at maturity (at least 31 DAS). By measuring paired leaves from >15 plants each (WT n = 34 leaves, *jaw-D* n = 36 leaves), we observed that leaves undergo approximately a 400-fold increase in area from 8 DAS to maturity, yet the gross morphology is established by 8 DAS. Generally, the first two leaves of *jaw-D* form two ripples and these ripples are established in the live imaging experiment window, while WT leaves never form ripples (Figure 1A-B, G, Supplemental Figure 1H-I). WT and *jaw-D* leaves have the same median size at maturity (Figure 1H, Wilcox test $p > 0.05$). Other measurements of organ size between WT and *jaw-D* are likewise comparable (Supplemental Figure 1B-E). We calculated the relative area of the first and second leaves of WT and *jaw-D* plants to ask how variable within a single plant the leaf size could be. While the median value was not statistically significant between WT and *jaw-D* plants (1.09 WT versus *jaw-D* 1.10, Wilcox test $p > 0.05$), *jaw-D* exhibited a greater spread of potential relative areas, with more extreme values and statistically higher coefficient of variation (Feltz and Miller Asymptotic test p = 3.051466e-05), indicative of higher size vari-

ability induced by the *jaw-D* mutation (Figure 1I). Also remarkable, we found that the petiole of *jaw-D* is shorter than WT (Figure 1J, Wilcox test $p < .0001$). The petiole grows through anisotropic expansion, so this agrees with previous work that suggests differentiation-driven expansion is promoted by TCPs (and thus would be lacking in *jaw-D*) (Efroni et al., 2008).

We were curious how leaves with approximately the same starting and ending tissue material could have such distinct shapes, namely flattened in WT and curved in *jaw-D*. When we measured the first true leaves of WT and *jaw-D* plants grown until maturity, *jaw-D* leaves could not be flattened and therefore small tears at the margin had to be induced to measure leaf characteristics, as reported previously (Figure 1G-J) (Bresso et al., 2018). In our live imaging, starting at 6 DAS tissue curving becomes evident in *jaw-D* leaves (Figure 1A-B red arrows, Videos 1, 4-5). This tissue curving continues throughout the experiment and is accompanied by ruffling along the margin at 8 DAS (Figure 1A-B, G, black arrows). We thus aimed to associate the spatial and temporal initiation of this curvature with cellular growth, division and differentiation patterns.

While WT leaves progressively flatten, jaw-D *leaves exhibit a proximal-distal distribution of curvature*

To quantify the magnitude and direction of tissue curvature, we calculated the Gaussian curvature for live imaged WT and *jaw-D* samples (Figure 2, Supplemental Figure 2). The type of curvature is represented by the sign, indicating a hill or valley (positive) or saddle (negative) structure. Therefore, values of Gaussian curvature further from zero indicate greater curvature in a region and changes in sign between regions indicates a change in the nature of the curving shape and greater tissue complexity. Extreme values in curvature at the curved leaf margin do not suggest differences between WT and *jaw-D.* In comparing early time points (3-5 DAS), WT leaves exhibit a larger spread of curvature values. This is perhaps due to the more pronounced formation of the petiole in these samples. At 6 DAS, however, the curvature of *jaw-D* samples spread distinctly between positive and negative values between proximal and distal halves, respectively, and show a large spread along the medial-lateral axis (Figure 2). At the same time, WT curvature values along the length and width tighten around 0, as the leaf flattens. We conclude that *jaw-D* curvature enhances throughout the leaf, not just at the margin and that this is initiated at 6 DAS.

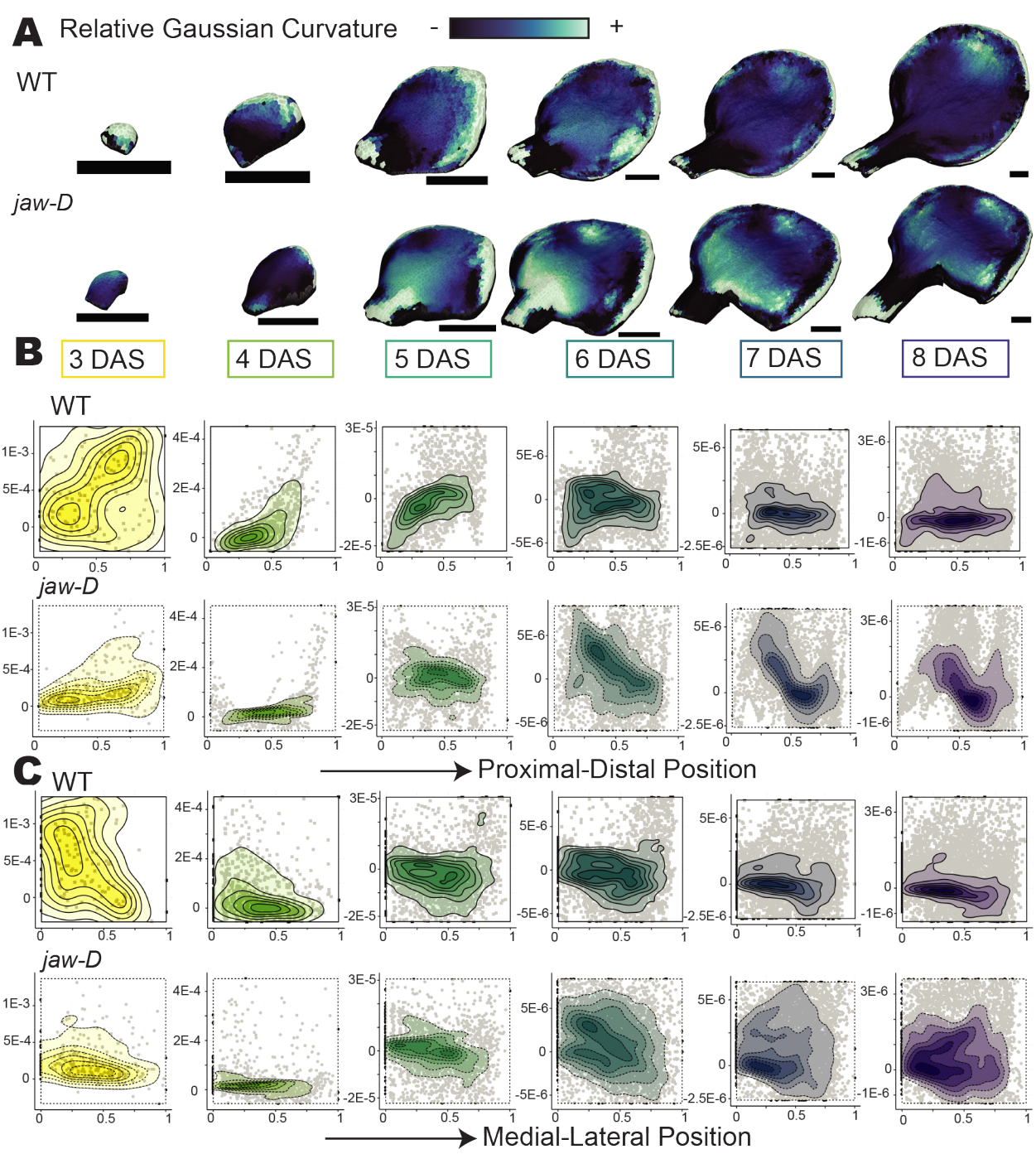

Figure 2. | While WT leaves progressively flatten, *jaw-D* leaves exhibit a proximal-distal distribution of curvature. (A) Gaussian curvature displayed as heatmaps on sample WT (top) and *jaw-D* (bottom) leaf meshes. Gaussian curvature represents both the magnitude and direction of curvature such that values further from zero represent greater curvature. Black bars = 200 µm. (B-C) Quantification of the distribution of curvature along the proximal-distal (B) and

We wondered if enhanced curvature in *jaw-D* might reflect the inability of *jaw-D* leaves to reconcile contrasting cellular growth and division along the lamina.

Growth variability is nearly indistinguishable between WT and jaw-D *locally*, *but is much higher globally across WT organs*

We chose to quantify growth heterogeneity locally and globally to test our hypothesis that distinct organ-wide regions of growth in WT are essential for the leaf flattening that is lacking in *jaw-D*. We first quantified local growth variability within cell lineages (temporal variability) or for each cell and its neighbors (spatial variability) using established methods (Hong et al., 2016). We found that WT and *jaw-D* are largely indistinguishable in their local spatial and temporal growth variability (Figure 5A-D). Stomata have recently been suggested as the source of most growth heterogeneity in tissues (Le Gloanec et al., 2022). However, our analysis was largely unaffected when stomata were excluded (Supplementary Figure 5). We next applied a cellular Fourier analysis to quantify the heterogeneity in growth of the tissue across all length scales (Figure 5E-F) (Fruleux and Boudaoud, 2021). This analysis verified our observations that *jaw-D* exhibits a slightly more homogenous distribution of growth across the leaf. Our cellular Fourier analysis also emphasized that the globally heterogeneous growth present in WT and lacking in *jaw-D* is only prevalent at 4-6DAS, when the curvature in *jaw-D* is established (Figure 5E black boxes, Figure 2). Given this co-occurrence, we hypothesized that organ-wide growth heterogeneity was responsible for flattening the WT leaf. We wondered if this early growth heterogeneity was developmentally regulated. We hypothesized developmental regulation of growth heteroge-

---

medial-lateral (C) axes for all three replicates of WT (top, squares, solid lines) and *jaw-D* laminas (bottom, circles, dashed lines). A proximal-distal gradient and broad lateral complexity of curvature is evident at 6 DAS in *jaw-D* leaves indicative of the broad proximal region that causes *jaw-D* leaves to curl. Note, as all leaves flatten, the Gaussian curvature changes dynamically over multiple orders of magnitude during the experiment. Further, the petiole and margin are sources of extreme outliers in curvature. Therefore, the scale for the heatmaps and graphs representing each time point has been calculated to encompass the 85% range of curvature values around the mean for that time point.

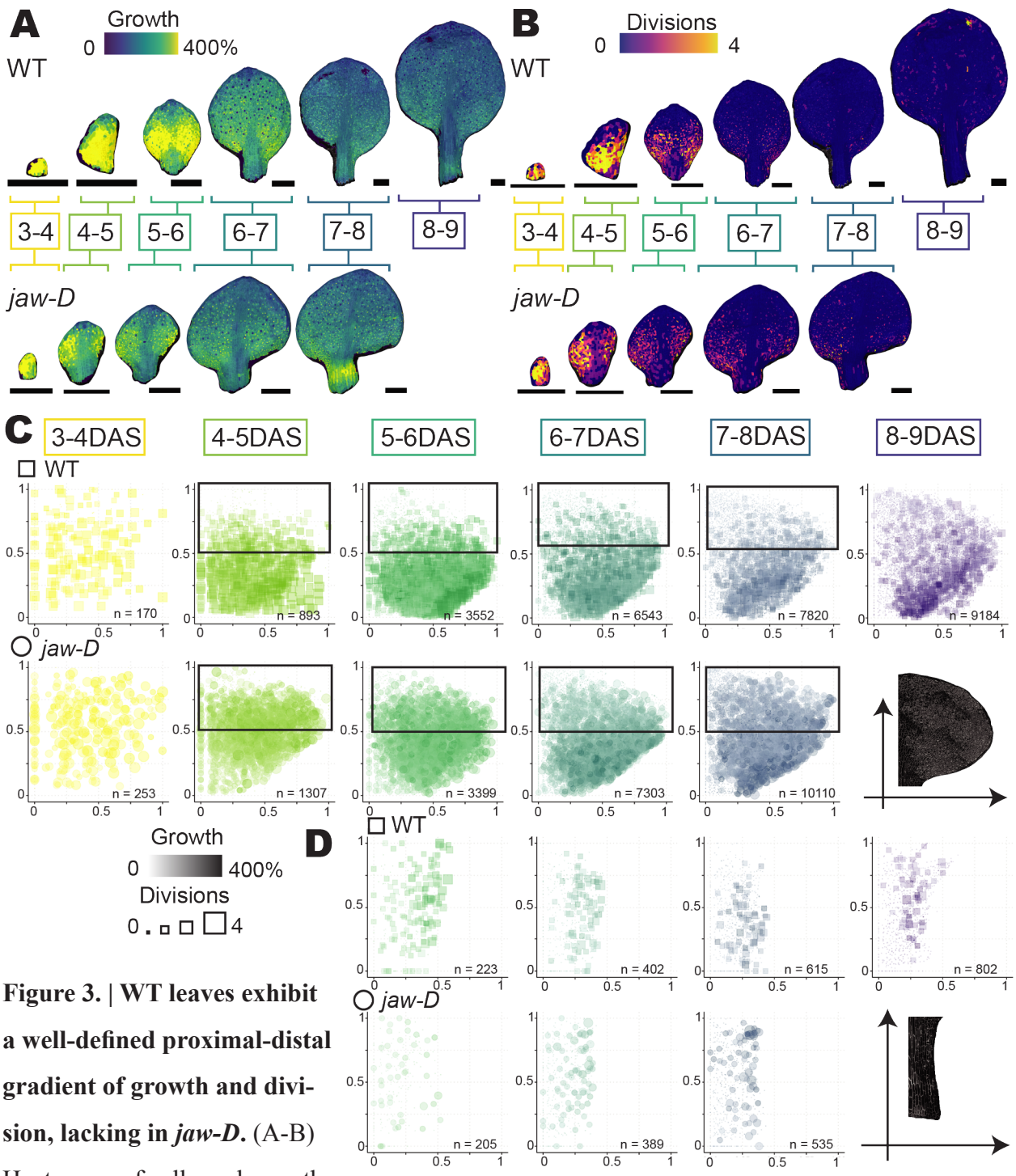

Figure 3. | WT leaves exhibit a well-defined proximal-distal gradient of growth and division, lacking in *jaw-D*. (A-B) Heat-maps of cell areal growth (A) and cell divisions (B) in 24 hour imaging periods represented on sample WT (top) and *jaw-D* (bottom) leaf meshes on the earlier time step. WT exhibits a distinct region of high growth and many divisions near the base (yellow coloring). This pattern is maintained over time, though the maximum value dynamically decreases with time. *jaw-D* areal growth and divisions are gen-

neity would be evident through the size of clonal sectors (decrease in size from base to tip) and cell morphology differences across the tissue.

WT leaves exhibit a well-defined proximal-distal gradient of growth and division, which is lacking in jaw-D

To investigate the relationship of cells to organ-level curving, we analyzed the patterns of cellular growth and division in the leaf. From our segmented and lineage tracked cells in each mesh, we calculated the growth rate (relative change in area) and number of divisions undergone by each cell at each time point in the live imaging experiment (Figure 3). To explore the relationship between cell division and growth in tandem, we represent each of these parameters for each cell in its normalized proximal-distal and medial-lateral position (Figure 3C-D). During 3-4 DAS, in both WT and *jaw-D*, cells throughout the leaf lamina grow and divide rapidly so there is an even distribution of big, yellow points. At 4-5 DAS, cells at the distal tip of the WT leaf slow their growth and division (black boxes). Still, high growth and cell division rates are coupled near the proximal leaf base. Darker regions in the lower half of WT plots are evident, representing the proximal region of growth and division (Figure 3C, top row). This proximal distal pattern of growth and division becomes more distinct between the proximal and distal halves in WT leaves

---

erally lower with a less well-defined pattern across the proximal-distal axis. Black scale bars = 200um. (C-D) All cells tracked in all three laminas (C) or petioles (D) of WT (top, squares) or *jaw-D* (bottom, circles) samples. N indicates the number of cells in each panel. Colors indicate 24 hour time points. The x and y axes represent medial-lateral and proximal-distal positions, respectively, normalized between 0 and 1 for the given replicate and time point. The size and color intensity of each point represents the number of divisions and areal growth, respectively, a cell has experienced between imaging days. WT cells show a distinct region of growth and division (dark, big squares) in the lower half of the lamina starting at 5-6 DAS. While, *jaw-D* cells exhibit a broader and less intense region in the bottom three quarters of the lamina. (C) Boxed regions indicate expansion of growing and dividing cells into the upper half of *jaw-D* (below) from 4-8DAS versus WT (above). (D) Petioles of WT and *jaw-D* generally exhibit lower, uniform growth and division.

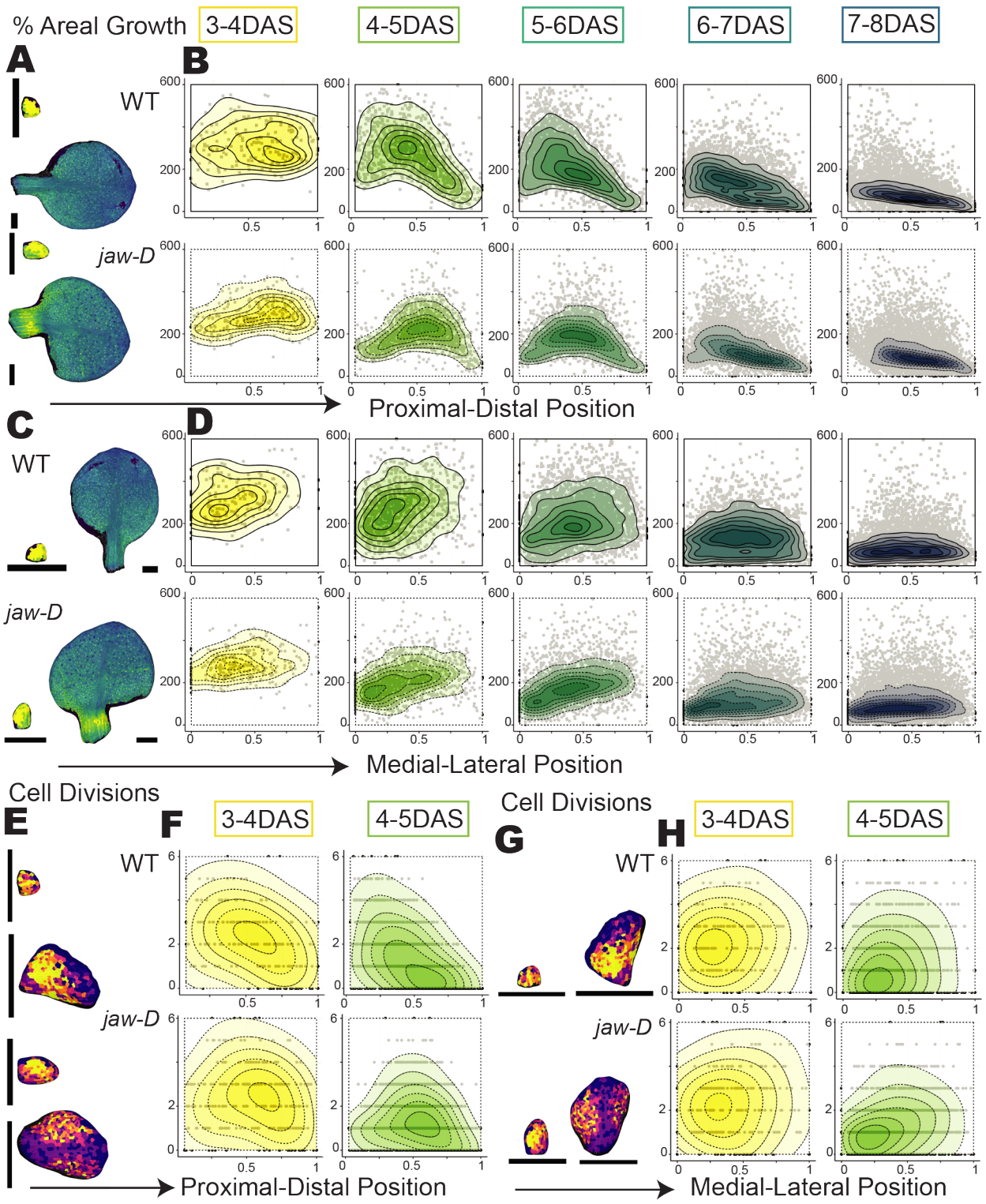

Figure 4. | The WT proximal-distal growth gradient, perturbed in *jaw-D*, could mediate variable medial-lateral growth present in both WT and *jaw-D* (A,C,E,G) Images reproduced from Figure 3 of areal growth (A,C) and cell division (E,G) on example WT (top) and *jaw-D*

through 8-9 DAS (compare boxed to unboxed regions). In contrast, this proximal-distal pattern is reduced in *jaw-D* leaves. The area where cell divisions and areal expansion occur is expanded distally starting at 4-5 DAS (boxed regions are more similar to unboxed). The distally expanded growth and division throughout the lamina in *jaw-D* is evident in the greater spread of dark colors and big sizes (Figure 3C, bottom row). Unlike the leaf blade, the petioles of all samples show more uniform growth and smaller number of divisions (Figure 3D). All three leaf replicates for each genotype exhibit these respective growth patterns (Supplemental Figure 3). We conclude that the basipetal growth gradient that is prominent in WT is perturbed in *jaw-D*.

To further quantify the defects in the basipetal growth gradient in *jaw-D*, we examined the level of daily growth and divisions along the proximal-distal axis of the leaf. We found a striking shift in the distribution of areal growth in *jaw-D* leaves along the proximal-distal axis. While, starting at 4-5 DAS WT shows a maximum of growth in the proximal quarter that decreases towards the tip, the maxima in *jaw-D* occurs near the middle to distal quadrant of the leaf (Figure 4 A-B).

(bottom) sample meshes. Images represent the first and last time points in subsequent graphs and are aligned to the developmental axis represented on the x-axis of the corresponding graphs. Black scale bars = 200 um. (B,D,F,H) Areal increase (B,D) or cell divisions (F,H) over one day intervals versus position along the proximal-distal axis (B,F) or medial-lateral axis (D,H) for each cell in all three WT (top, squares, solid lines) or *jaw-D* (bottom, circles, dotted lines) lamina replicates. WT and *jaw-D* are broadly similar from 3-4 DAS. At 4-5 DAS, WT growth and divisions begin to exhibit a proximal-distal gradient with a proximal maximum, while *jaw-D* growth and divisions are lower and the maximum is more central. WT and *jaw-D* are largely similar in growth and divisions along the medial-lateral axis though WT has a slightly larger spread of growth values and *jaw-D* has a narrower spread with both exhibiting a slight tilt of increased growth in lateral regions starting at 4-5 DAS. (E-F) Cell divisions largely follow the trends in growth along the proximal-distal axis. However, *jaw-D* lacks increased cell divisions laterally and most divisions end at 4-5 DAS (G-H). Use of density plots, coloring, and axis normalization as in Figure 2.The ranges of the y-axis in the plots are chosen for better visualization of the dominant features in the displayed distributions.

These patterns are maintained through 5-6 DAS, then at 6-7 DAS *jaw-D* shifts to a more WT growth profile. This suggests that a regulatory signal perceived by WT cells at 3-4 DAS to induce the growth gradient at 4-5 DAS is not perceived by *jaw-D*. Cell divisions showed similar trends (Figure 4E-H) with the *jaw-D* distribution centered near the middle half and the WT distribution decreasing from a maximum in the proximal quarter of the leaf. Thus, the growth and division gradient of WT is relatively flattened with moderate growth and division rates extending further across the *jaw-D* leaf.

The suppression of the basipetal growth gradient in *jaw-D* is consistent with the current understanding of disruption of the *miR319 TCP* network in *jaw-D*. TCP transcription factors promote maturation from the tip downward (Schommer et al., 2008; Efroni et al., 2008; Bresso et al., 2018; Sarvepalli and Nath, 2011). Ectopic expression of *miR319* leads to expanded repression of *TCP* expression and consequently suppresses the basipetal growth gradient in our live imaging analysis.

We were struck by the observation that the *jaw-D* leaf does not become longer than WT (Figure 1D) despite having an expanded region of fast growth and division (Figure 4B). To explore how contrasting spatial growth profiles for WT and *jaw-D* genotypes can lead to overall similar leaf length dynamics, we created a simple one-dimensional model to capture the length of the leaf over time. In the model, we assume growth is initially exponential in both WT and *jaw-D*. As the leaf dynamics exit this initial exponential phase, growth becomes a function of both time and spatial location and also becomes different between WT and *jaw-D*. For WT, we implement a growth curve in which growth decreases with increasing distance from the leaf base (Supplemental Figure 4E). We also assume that the growth at the leaf base decreases over time; this decrease is essential to eventually stop all growth as the leaf length approaches its steady-state value. We simplify the *jaw-D* growth profile to be a constant moderate growth rate along the leaf length (Supplemental Figure 4E). Consistent with our data, the model predicts similar leaf lengths can be maintained between WT and *jaw-D* (Supplemental Figure 4F). Based on the model, we conclude that different proximal distal growth patterns can yield similar leaf lengths.

In first leaves, curvature is not attributed to overgrowth at the jaw-D leaf margin

We wondered about the relative contribution of growth along the margin versus the proximal-distal gradient disruptions we observed in enhancing the curvature of *jaw-D* leaves. In previous publications, leaf ruffling has been attributed to overgrowth along the leaf margins (Avery, 1933; Alvarez et al., 2016). We examined the level of daily growth and divisions separately along the medial-lateral axis to determine how the dynamics and distribution of these behaviors relate to the induction of curvature we observed at 6 DAS in *jaw-D* (Figure 4). There is a greater spread in the relative medial-lateral growth in WT than in *jaw-D* (broader contour shape, Figure 4C-D). Along the medial-lateral axis, both WT and *jaw-D* exhibit a slight lateral tilt in magnitude while *jaw-D* shows a narrower distribution of growth values starting at 4-5 DAS. The growth in lateral *jaw-D* regions is equal to or less than WT growth, suggesting overgrowth of the margin is not the major cause of curvature, at least in leaf 1. Cell divisions largely cease at 5-6 DAS and are less distinguishable medio-laterally between WT and *jaw-D* (Supplemental Figure 4A-B). So, we reasoned that growth, rather than divisions, was a major driver in creating the curvature differences in *jaw-D* leaves. We note that our live imaging captured the first of ultimately two ripples that will be formed in the first leaves of *jaw-D* (Figure 1B and G), which is fewer than later developing leaves. We also note that we use the term ripple, because the phenotype is not just at the margin, but curvature that extends across the whole leaf. We do not exclude the possibility that later developing leaves with more ruffles additionally exhibit overgrowth of the margins. However, our analysis shows that the rippling leaf curvature of *jaw-D* can occur in the first two leaves without growth at the leaf margins distinct from WT.

Growth variability is nearly indistinguishable between WT and jaw-D *locally*, *but is much higher globally across WT organs*

We chose to quantify growth heterogeneity locally and globally to test our hypothesis that distinct organ-wide regions of growth in WT are essential for the leaf flattening that is lacking in *jaw-D*. We first quantified local growth variability within cell lineages (temporal variability) or for each cell and its neighbors (spatial variability) using established methods (Hong et al., 2016). We found that WT and *jaw-D* are largely indistinguishable in their local spatial and temporal growth variability (Figure 5A-D). Stomata have recently been suggested as the source of most

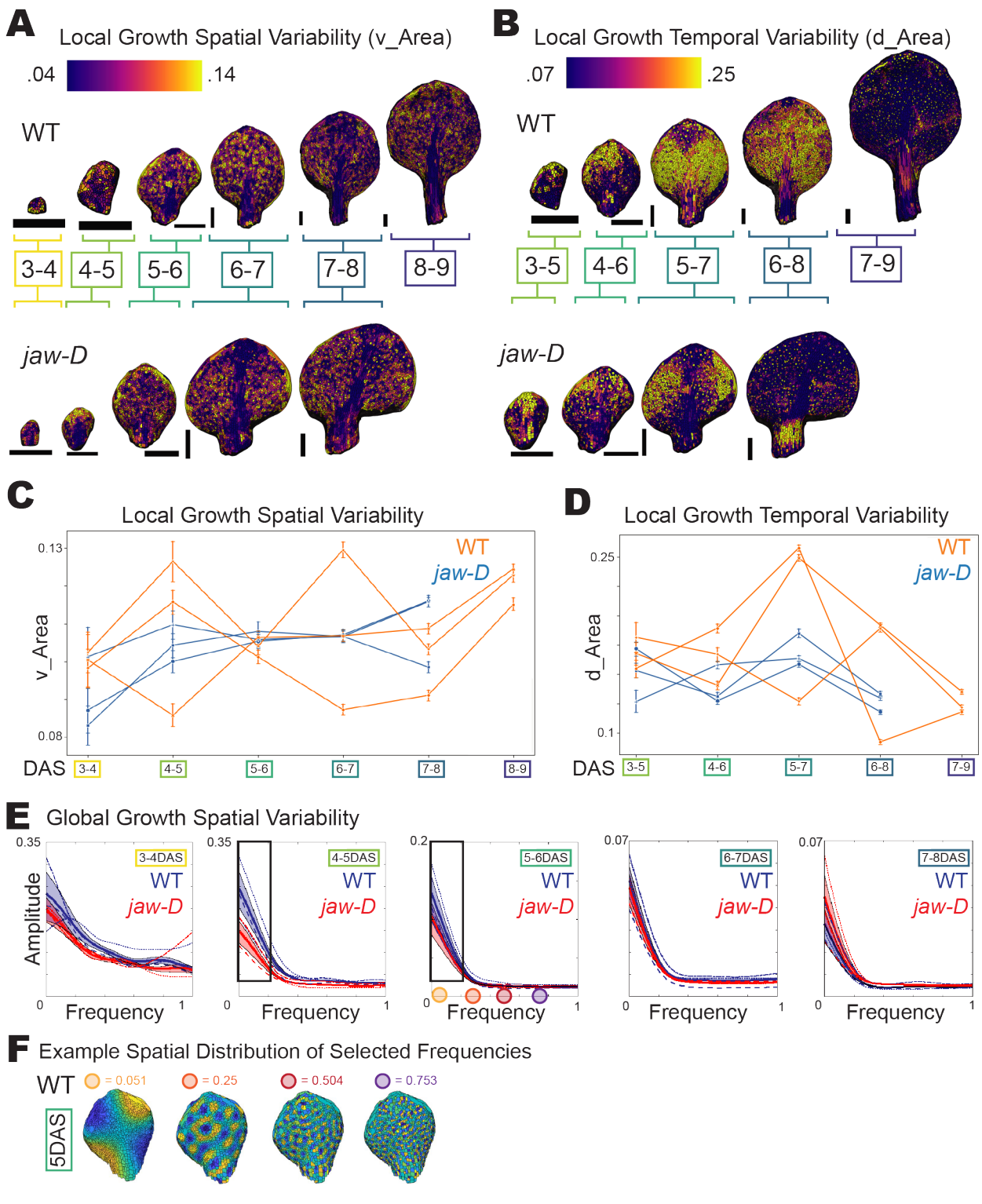

Figure 5. | Global growth variability dominates in WT leaves (A) Heat-maps of local spatial growth variability over 24 hour windows represented on sample WT (top) and *jaw-D* (bottom) leaf meshes on the earlier time step. (B) Heat-maps of local temporal growth variability in 48

growth heterogeneity in tissues (Le Gloanec et al., 2022). However, our analysis was largely unaffected when stomata were excluded (Supplementary Figure 5). We next applied a cellular Fourier analysis to quantify the heterogeneity in growth of the tissue across all length scales (Figure 5E-F) (Fruleux and Boudaoud, 2021). This analysis verified our observations that *jaw-D* exhibits a slightly more homogenous distribution of growth across the leaf. Our cellular Fourier analysis also emphasized that the globally heterogeneous growth present in WT and lacking in *jaw-D* is only prevalent at 4-6DAS, when the curvature in *jaw-D* is established (Figure 5E black boxes, Figure 2). Given this co-occurrence, we hypothesized that organ-wide growth heterogeneity was responsible for flattening the WT leaf. We wondered if this early growth heterogeneity was developmentally regulated. We hypothesized developmental regulation of growth heterogeneity would be evident through the size of clonal sectors (decrease in size from base to tip) and cell morphology differences across the tissue.

Cell differentiation quickly propagates from the distal tip along the leaf length in WT, unlike jaw-D

We turned to clonal sector analysis of cells that could be mapped from the 8 DAS leaf back to their early progenitors at 4 DAS to understand how differences in growth patterns between WT

---

hour windows, represented on sample WT (top) and *jaw-D* (bottom) leaf meshes on the middle time step. Black scale bars = 200 um. (C-D) Quantification of the mean (C) local growth spatial variability or (D) local growth temporal variability for time windows as in (A-B). Individual lines connect mean values for each of three WT (orange) or *jaw-D* (blue) replicates. Error bars indicate standard error of the mean. WT and *jaw-D* local spatial and temporal growth variability are largely indistinguishable, though *jaw-D* replicates are generally tighter around the mean. (E) Global spatial variability of areal growth for 24 hour windows determined through cellular Fourier analysis. High amplitudes at lower frequencies represent higher variability at larger length scales. Lines represent each of three WT (blue) or *jaw-D* (red) replicates with root mean squared error shaded. At 4-5DAS and 5-6DAS WT leaves exhibit much higher variability in growth across the organ than *jaw-D* (boxed). (F) Example of spatial range for different frequencies displayed on 5DAS WT leaf. Colored dots indicate the frequency value on the x-axis of (E) panel 3.

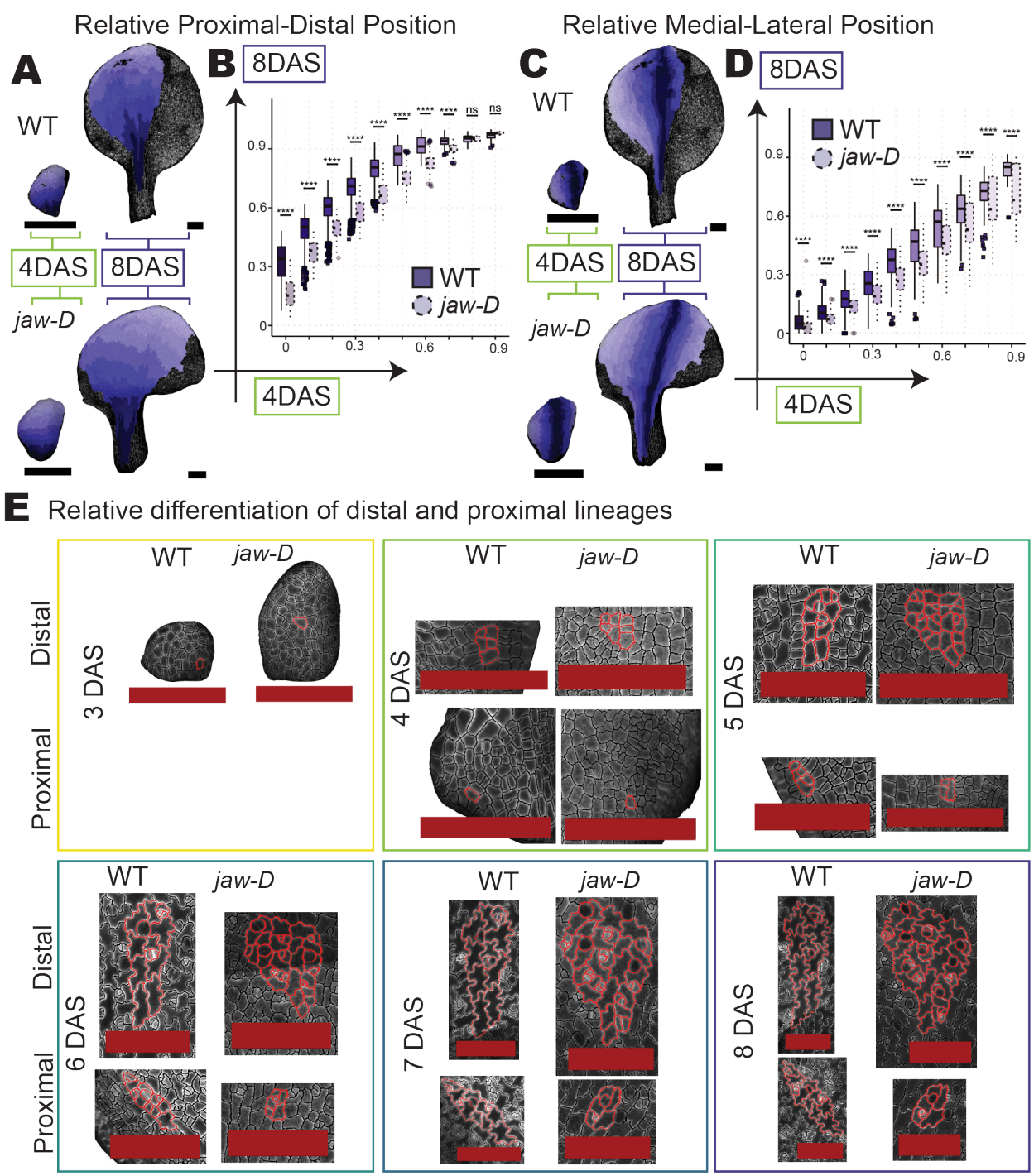

Figure 6. | Cell differentiation quickly propagates from the distal tip along the leaf length in WT, unlike *jaw-D*

(A, C) Clonal analysis of WT (top) and *jaw-D* (bottom) cells mapped from 4 DAS to 8 DAS on sample leaf meshes. Clonal sectors (shades of purple) were binned evenly at 4 DAS into ten proximal-distal (A-B) or medial-lateral (C-D) sectors. Uncolored cells could not be tracked

596 and *jaw-D* correspond with maturation of different tissue locations (Figure 6A-D, Videos 2-5).
597 Progenitor cells were assigned into 10 even proximal-distal (Figure 6A-B) or medial-lateral (Fig-
598 ure 6C-D) bins based on their position at 4 DAS. Then their locations at 8 DAS were compared.
599 4 DAS proximal regions had a much greater contribution to 8 DAS leaves in WT (darker purple
600 coloring in Figure 6A or steeper curve in 6B) than *jaw-D* (more even coloring and shallower
601 curve in 6A,B). Yet, the most distal two tenths of both WT and *jaw-D* leaves had the same mean
602 position from 4 DAS to 8 DAS, suggesting that this region of the leaf identity may be unper-
603 turbed in *jaw-D. Jaw-D* also showed a slight shift in the contribution of more lateral cells to the
604 final leaf width (Figure 6C-D). Note, we also performed this analysis from 3 DAS to 8 DAS, but
605 so much of the final leaf is contributed from the base in WT that only about half of the leaf could
606 be back-tracked (Supplemental Figure 6). The proximal-distal patterns still largely held, however
607 the medial-lateral differences were much less pronounced. Models of leaf flatness have suggest-
608 ed that long range coordination could be necessary to deal with the variable forces present in
609 the lamina (al-Mosleh and Mahadevan, 2022; Derr et al., 2018). Thus, we hypothesized that the
610 disrupted flatness of *jaw-D* leaves could be attributed to disrupted coordination of organ sectors.
611

---

612 between all time points. (A) Darker purple WT bins end up larger than lighter bins indicative of
613 expanded contribution of proximal growth and divisions to the overall leaf versus, a more even
614 distribution of colors in *jaw-D.* Black scale bars = 200 µm. (C) Lighter purple bins are expanded
615 in *jaw-D* indicating a lateral shift of sector contributions. (B,D) Quantification of proximal-distal
616 (B) or medial-lateral (D) sector relationships for 4 DAS sector bins mapped to 8 DAS positions
617 for all three replicates of WT (left, dark shading, solid lines) and *jaw-D* (right, light shading,
618 dotted lines) whole leaves. Boxes indicate the 75% interquartile range, middle bar represents me-
619 dian, whiskers represent outliers and squares (WT) or circles (*jaw-D)* represent extreme values.
620 Nearly all 4 DAS sector bins have different mapping to 8 DAS positions between WT and *jaw-D*
621 representing more prominent contributions of WT proximal and medial regions than disbursed
622 and lateral contributions in *jaw-D* ($p<.0001$, paired Student's t-test and Bonferroni correction).
623 (E) Tracing the same proximal (bottom) and distal (top) cell lineages (red outlines) for the entire
624 experiment for WT (left) or *jaw-D* (right) sample leaves. WT cells exhibit greater differentiation
625 into lobed pavement cells starting at 5 DAS. Red scale bars = 100 µm.

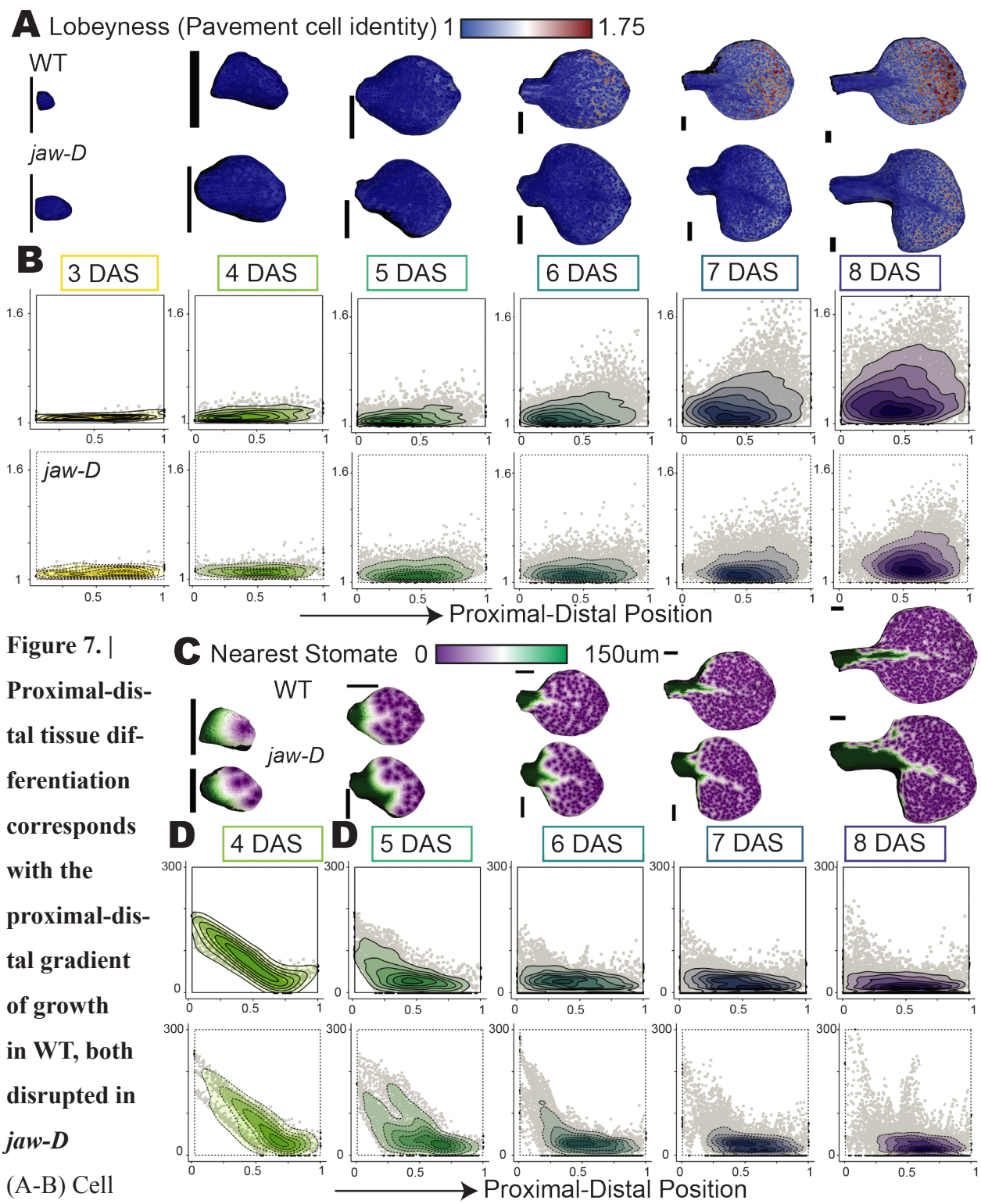

Figure 7. | Proximal-distal tissue differentiation corresponds with the proximal-distal gradient of growth in WT, both disrupted in *jaw-D*

(A-B) Cell lobeyness (the perimeter of a cell divided by its convex hull, a measure of pavement cell differentiation). Represented as heatmaps (A) on sample WT (top) or *jaw-D* (bottom) leaf meshes for each day of the

Proximal-distal tissue differentiation corresponds with the proximal-distal gradient of growth in WT, differentiation is correspondingly disrupted in jaw-D

We wanted to understand how these sectoral patterns relate to cell differentiation phenotypes. We used cell lobing as a measure of the differentiation of pavement cells (Sapala et al., 2018; Tsuge et al., 1996). We chose two lineages with approximately equal beginning and ending positions between WT and *jaw-D* to track over the entire experiment, a distal lineage that emerged at 3 DAS and a more proximal lineage that emerged at 4 DAS (Figure 6E). This comparison revealed how differentiation signals are more acutely experienced by WT leaves as the pavement cell lobing increased starting at 5 DAS in the distal lineage and 6 DAS in the proximal lineage. Whereas, lobing in the *jaw-D* lineage began at 6 DAS, never became as elaborate as WT lobing, and further, was more similar between distal and proximal lineages. From this specific example, we wanted to expand our focus to tissue-wide differentiation.

The differences in pavement cell lobing observed in single lineages motivated us to measure global changes in the distribution of cellular differentiation relative to the growth front we measured in WT versus *jaw-D.* We measured pavement cell lobing and stomatal characteristics to un-

---

imaging experiment. Black scale bars = 200 µm. (B) Lobeyness versus position along the proximal-distal axis for each cell in all three WT (top, squares, solid lines) or *jaw-D* (bottom, circles, dotted lines) lamina replicates. Lobeyness is initiated at the distal tip of WT cells at 5 DAS and increases while propagating down to the leaf base. Increases in lobeyness are subtler, later and more disbursed in *jaw-D* samples. (C-D) Stomatal spacing (the distance in µm to the nearest stomate from any pavement cell, the inverse of stomatal density) (C) represented as heatmaps on sample WT (top) or *jaw-D* (bottom) meshes for each day of the imaging experiment. (D) Quantification of stomatal spacing across laminas with plotting as in (B). Note, stomata first initiate at 4 DAS. Stomatal spacing quickly tapers in WT as stomata are initiated and become evenly distributed through the lamina. There is a slight proximal lag in this process in *jaw-D,* though much less pronounced than lobeyness suggestive of separable patterning processes. Use of density plots, coloring, axis selection and normalization as in Figure 4.

derstand how two different types of differentiation proceed in the cells of WT and *jaw-D* leaves (Figure 7). The Lobeyness measure in MorphoGraphX allows us to ascertain the level of lobing present in segmented cells throughout the epidermis of a given leaf. We used this measure to ask how patterns of differentiation present along the proximal-distal and medial-lateral axes change with leaf development. We found that in WT leaves, lobing begins to increase in the distal quarter of the leaf at about 5 DAS. Over subsequent days, the lobeyness of many of these distal cells continues to increase and lobeyness initiation propagates from tip to base. (Figure 7A-B). In contrast, *jaw-D* leaf cells initiate lobing 6 DAS or later, to a lesser extent and more evenly along the length of the leaf, suggesting differentiation is reduced in *jaw-D.* Along the medial-lateral axis, the differences in absolute magnitude of cell lobing are especially clear between WT and *jaw-D* samples (Supplemental Figure 7). This suggests that important differentiation signals at 5 DAS that are perceived in WT, perhaps to reinforce and structure the growth directions, are lacking in *jaw-D.*

Stomata also initiate as leaf tissue matures, so we wanted to investigate if stomatal production was also impaired in *jaw-D.* In contrast to pavement cell lobing, we did not see such stark differences between WT and *jaw-D* in stomatal density (Figure 7C-D). We measured stomatal density by labeling each stomate (labeled as one cell) in each leaf and then calculated the distance from any pavement cell to the nearest stomate. At 4 DAS the spacing curve is nearly the same between WT and *jaw-D* as the first stomata are initiated at the tip. There is a slight lag in the flattening of this curve in *jaw-D* as stomatal initiation waves down the growing lamina at 5 and 6 DAS. Yet, by 7 and 8 DAS both WT and *jaw-D* have evenly spaced stomata. We hypothesize this indicates the physiological importance of properly spaced stomata and the independence of this process from tissue and organ-wide shape regulation. However, we found that though evenly spaced, stomata in *jaw-D* were smaller and rounder, while WT stomata begin to grow anisotropically and increase exponentially in size along the proximal-distal axis, (Supplemental Figure 8). This suggests that while stomatal initiation is maintained in *jaw-D*, stomatal maturation is also perturbed. Since cellular differentiation appears perturbed in *jaw-D* and *jaw-D* leaves are not flat, we concluded that a proper cellular differentiation gradient could be important for leaf organ flattening. It has been observed that pavement cell lobeyness can mediate tissue stresses imposed by isotro-

pic growth. We propose that this pavement cell maturation pattern could be important for permitting dynamic growth coordination in WT.

WT cells can dynamically polarize their growth to shape early leaves; this control is lacking in jaw-D

To assess how regions of growth and differentiation might guide organ flattening in WT leaves, we measured the relative growth difference between maximal and minimal directions of each cell, a version of anisotropy (Figure 8). We calculate this by determining the cellular junctions between which the maximal growth occurs and the growth in the perpendicular (inherently minimal) direction. We then subtract these values to get a measure of anisotropy, i.e. if a cell is growing isotropically these measures are equal, so isotropic cells have a value of 0. We found that the distribution of WT anisotropy mimics the WT growth gradient pattern with a graded pattern starting at 4-5 DAS until 7-8 DAS (Figure 8A-B). As cell growth and division slows from the tip, anisotropy decreases in magnitude in WT. At 8-9 DAS growth in WT leaves exhibits the same level of anisotropy throughout the lamina (Supplemental Figure 9). Anisotropy in *jaw-D* also follows its respective growth pattern. It is spread from 0 (isotropic) to around 1 along the length of laminas. As with growth, there is a maxima of anisotropy located in the center of the leaf length at 4-5 DAS and 5-6 DAS with a return to a more WT-like distribution from 6-7 DAS onwards. Anisotropy is generally lower in *jaw-D* than wild type. This could help explain the shorter petiole phenotype we observed in mature *jaw-D* leaves, since petioles invoke anisotropic growth to elongate (Figure 1J). We computed the anisotropy over spatial scales as before with a cellular Fourier analysis (Figure 8E). This analysis concurs with our observations that WT heterogeneity in anisotropy is greater at large spatial scales than *jaw-D,* especially from 4-6DAS.

We then wondered if the orientation of the anisotropy relative to the leaf axis was important for flattening. We calculated the difference between the growth oriented along the proximal-distal axis minus the growth orthogonal to this axis (Figure 8C-D). With this calculation values of 0 indicate isotropic growth between proximal-distal and medial-lateral axes, positive values indicate alignment of maximal growth with the proximal-distal axis and negative values indicate alignment of maximal growth in the medial-lateral direction. This confirmed that the alignment

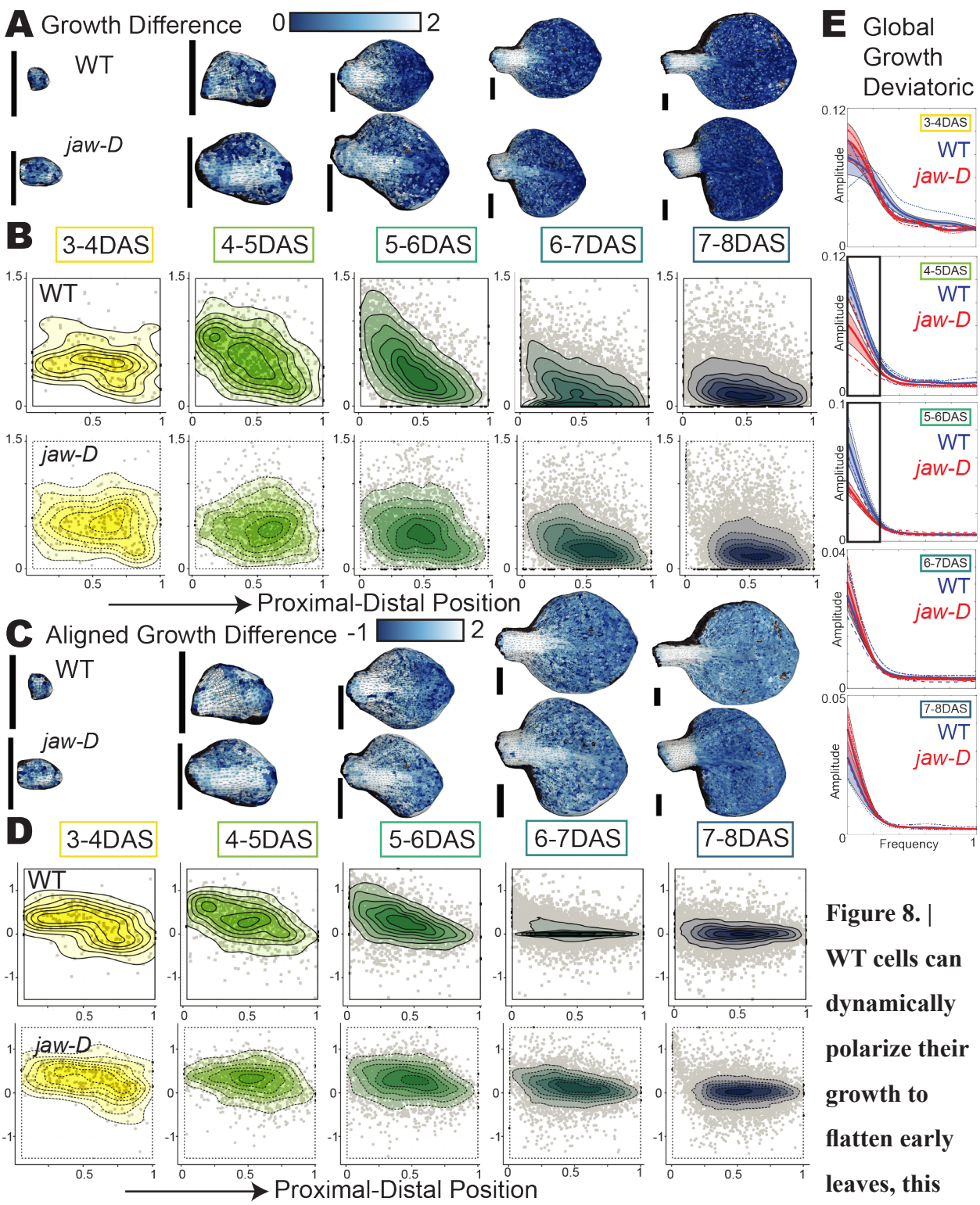

Figure 8. | WT cells can dynamically polarize their growth to flatten early leaves, this control is lacking in *jaw-D*. (A) Lines indicate the direction of maximal and minimal growth tensors shown for each cell scaled to the magnitude of the growth (longer lines indicate more growth). Heatmap colors indicate the difference of maximal minus minimal growth in sample

of growth is dynamic in WT with a gradient of aligned anisotropy localized at the base from 3-5 DAS. It also highlighted a notable period of nearly isotropic growth with respect to the proximal-distal axis at 6-7 DAS only present in WT. In *jaw-D,* aligned relative growth hovers between -.05 and 1 for nearly all time points suggesting a preference towards alignment with the proximal-distal axis along the length of the leaf through 6-7 DAS. Further, at 7-8 DAS some anisotropy flips to orthogonal alignment in the same proximal-distal sectors which might enhance growth conflicts (Figure 8C-D).

We turned to finite element method (FEM) simulations to simulate how each of these patterns of anisotropic growth affect curvature. We followed previous models by dividing the leaf into small elements and using gradients of growth factors and tissue polarity to control the growth of individual elements (Kuchen 2012, Kierzkowski 2019), but without confining the simulation to a plane. The FEM was then used to resolve the conflicts that arise due to the differential expansion

---

WT (top) or *jaw-D* (bottom) leaves for each 24 hour interval shown on the earlier time point. Black scale bars = 200 µm. (B) Difference in growth (= growth in maximal direction - growth in minimal direction) versus position along the proximal-distal axis for each cell in all three WT (top, squares, solid lines) or *jaw-D* (bottom, circles, dotted lines) lamina replicates.Patterns in the distribution of the maximal growth anisotropy follow patterns in the respective growth gradients (See Figure 4). (C) Heatmap indicating difference in growth along the proximal-distal axis minus orthogonal growth on sample WT (top) or *jaw-D* (bottom) leaves for each day of the imaging experiment. Magnitude of growth along and orthogonal to the proximal-distal axis is indicated with lines as in (A). (D) Quantification of difference in aligned growth in laminas with plotting as in (B). WT cells can dynamically align their growth along different axes in different regions of the leaf at different times. Whereas, *jaw-D* growth is more often aligned along the proximal-distal axis. Use of density plots, coloring, axis selection and normalization as in Figure 4. (E) Cellular Fourier analysis of the deviatoric growth tensor, a tensor that quantifies growth anisotropy, across organ spatial scales (plotting as in Figure 4.5). WT leaves exhibit more heterogeneity in anisotropy organ-wide from 4-6 DAS, indicated by low frequencies with high amplitude (boxed).

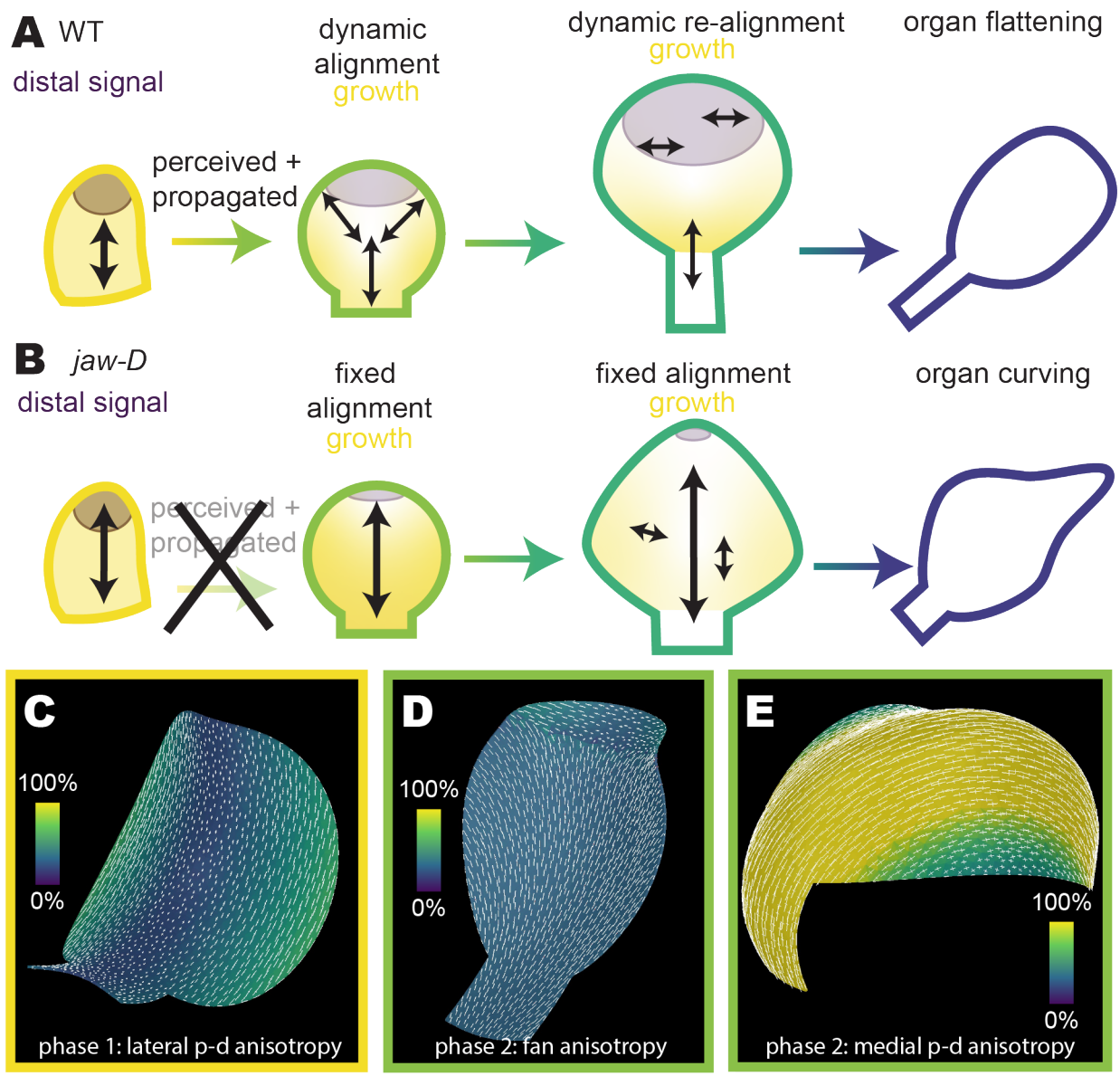

Figure 9. | A model for leaf flattening based on the dynamic re-alignment of leaf growth. All leaves experience an early differentiation signal that defines the distal tip of the leaf. (A) In WT, this signal is reinforced through the permissiveness towards isotropy that distal differentiation permits. Meanwhile, the initial alignment of growth along the proximal-distal axis becomes progressively restricted to the petiole region. This allows leaf widening and expansion, while remaining flat. (B) *jaw-D* exhibits a weaker response to this signal; growth remains aligned with the entire length of the leaf. This fails to resolve growth conflicts between the slower growing leaf center and faster growing leaf edge which, coupled with anisotropy patterns cause of the curvature to increase and ripples to form in the lamina. Growth level indicated in yellow shad-

of individual elements, leading to the emergent shape of the leaf structure. Both WT and *jaw-D* leaf primordia initiate with proximal-distal growth alignment across the leaf (Figure 8C-D; Figure 9A-B). We created a model with low anisotropic growth (along the proximal-distal axis) at the midrib and higher anisotropic growth at the margins. Simulation of this model created a leaf primordium that arches back (Figure 9C; Video 6), similar to the way the young leaf primordium arches slightly back from meristem (Figure 1A 4 DAS). Next the WT leaf growth anisotropy rearranges dynamically to generate a fan pattern from the base of the lamina, while growth slows at the tip (Figure 8C-D; Figure 9A). We simulated this pattern with anisotropic growth in the basal portion, but the direction rotating in cells nearer the margins. Simulation of this model produced a relatively flat expanding leaf until the growth conflicts pushed the tip out of plane (Figure 9D; Video 7). In contrast to WT, *jaw-D* maintains a strong band of anisotropic growth in the middle of the leaf during this phase (Figure 8C-D; Figure 9B), as if *jaw-D* leaves persist in the earlier phase of growth longer. We created a model that has strong anisotropic growth at the midrib, and low anisotropic growth near the margins. Simulation of this model produced a strongly curved slightly cupped leaf (Figure 9E; Video 8 at 5 sec). When the simulation was allowed to run longer, the leaf curled over on itself (Video 8 at 11 sec). Without the cover slip used for imaging, *jaw-D* leaves curl over on themselves (data in pending manuscript). In this model, the whole leaf curls, not just the margins, which is consistent with our images of the jaw-D (Figure 1B, Figure 2). In the third phase both leaves grow isotopically (Figure 8C; Figure 9A-B). We note that in all of these models, extended simulation time leads enhanced curvature (Videos 6-8), suggesting that dynamic realignment of growth over development is crucial for maintaining wild-type leaf flatness. Further, our models suggest that it is the growth conflicts that accumulate from the per-

---

ing, distal signal propagation in purple, growth alignment in black arrows and leaf age in outline color. (C-E) FEM simulations of leaf mesh growth with different spatial distributions of anisotropic growth. Color indicates growth ratio, lines indicate anisotropy direction. (C) Phase 1 with proximal-distal anisotropic growth high laterally. (D) WT-like phase 2 with anisotropy fanning out from the base of the leaf. This anisotropy pattern permits flattening. (E) *jaw-D*-like phase 2 with anisotropy high near the midrib across the length of the leaf. This anisotropy pattern induces curvature.

sistence of highly anisotropic growth in *jaw-D* that leads to curvature of the whole leaf.

We conclude, therefore, that it is the ability of WT cells to dynamically re-orient their growth that allows flattening, and conversely the inability of *jaw-D* cells to re-orient their growth that contributes to curvature throughout the leaf.

Discussion

With this work, we shed new light on how the regulated juxtaposition of different growth programs along the length of WT leaves allows initially round organs to grow flat and how the disruption of this growth coordination causes *jaw-D* leaves to curve. By conducting live cellular imaging on the same leaves from first initiation through a 400-fold increase in area and 100-fold increase in cell number over six days, we have captured an immense level of detail of this process (Figure 1). We found that disruptions in tissue curvature in *jaw-D* become evident at 6 DAS (Figure 2). This curvature increase immediately follows a growth program disruption, wherein *jaw-D* exhibits a pattern of medium growth broadly extending along most of the length of the leaf. Whereas, WT exhibits a proximally localized maxima and slowing growth gradient towards the tip (Figure 3-4). It is also at 5-6 DAS that important shifts in cellular differentiation become obvious in WT leaves with pavement cells in the distal quarter of the leaf increasing greatly in their lobing (Figure 6-7). Just before these tissue maturation transitions, a notable juxtaposition of proximal-distally aligned anisotropic growth in the proximal half and isotropic growth in the distal half exists in WT laminas – and is missing in *jaw-D* (Figure 8). Based on this information, we propose a model wherein, WT leaves perceive and propagate distal differentiation signaling to initiate and maintain two different growth alignments between proximal and distal halves. These cellular behaviors combine to allow WT leaves to remain flat while rounding along the margin (Figure 9). Our model complements recent observations that spatially specific reinforcement of tissue stresses may occur in three dimensions to promote organ flattening (Zhao et al., 2020).

Our data clarifies how the *jaw-D* mutant can have dramatic phenotypic changes along the margin and in three dimensions while the underlying genetic players function along the proximal-distal

axis of the lamina. The miRNA overexpressed in *jaw-D,* miR319*,* is expressed from the base of leaves and floral organs (Nag et al., 2009). Its expression from the base limits class II TCP transcription factor presence to distal regions (Challa et al., 2019; Palatnik et al., 2003). Our growth data agrees well with this model in WT as a region of fast growth and division is present at the base of WT leaves (Figure 3-4). Since *jaw-D* over-expresses miR319, and should therefore further decrease the presence of TCPs in the leaf, we expected there to be an increase in the size of the fast growth and division zone seen in WT. However, we were surprised to find that the change was more nuanced. Instead the growth rates were more moderate in *jaw-D* and distributed further along the proximal-distal axis. We noted that cell divisions followed the altered growth pattern in *jaw-D,* and that their contribution to the organ ends earlier than growth. We think that the distribution of contrasting growth along the medio-lateral axis in WT and *jaw-D* could induce conflicts between tissue regions (Figure 4). These conflicts may be resolved in WT by allowing for dynamic re-orientation of growth along the proximal-distal axis, which is lacking in *jaw-D* (Figure 8C-D).

Our surprising findings about the distribution of growth magnitude and orientation along the length of *jaw-D* leaves may be attributed to the greater importance of TCPs in guiding cellular differentiation to enable growth re-alignment, rather than growth repression per se (Figure 6-8) (Koyama et al., 2010, 2007; Sun et al., 2017; Efroni et al., 2008; Koyama et al., 2017). Our data on long term cell lineage tracing supports a model where a distal differentiation signal is present both in WT and *jaw-D* leaves, but *jaw-D* leaves are not able to interpret and coordinate development in response to this signal (Figure 6A-B). TCPs may be required for this signal perception. TCP4 has been associated with activating secondary cell wall biosynthesis (Sun et al., 2017). So, TCPs could also be crucial in reinforcing differential growth patterns by supporting the transition to differentiated cell identity that enables dynamic growth re-alignment from anisotropic to isotropic. Further, the lobing of pavement cells induced by differentiation is important for dispersing tissue stresses associated with isotropic growth (Sapala et al., 2018). Another likely consequence of this lack of differentiation can be seen in the shorter petioles of *jaw-D* (Figure 1J). Differentiation signal propagation may be necessary for the elongation of the petiole in WT leaves.

Our work complements findings outside of land plants that establish how mechanical instabilities can induce organ forms (Nelson, 2016). Studies in kelp suggest that the water flow stresses experienced by the same species in different environments determines blade ruffling or flattening (Koehl et al., 2008). In animals, intestinal and cranial folding out of the plane have been attributed to differential growth and buckling between membrane layers (Hannezo et al., 2011; Shyer et al., 2013; Ben Amar and Jia, 2013; Tallinen et al., 2016; Karzbrun et al., 2018). Work in Drosophila also concurs that the spatial distribution of differential growth is important in creating multiple folds of the wing disc epithelium (Tozluoğlu et al., 2019).

We also discovered an interesting difference between cellular differentiation programs. Namely, the differentiation of pavement cells is altered in *jaw-D,* while the initiation and spacing of stomata remains intact (Figure 7). This result highlights the diversity of differentiation programs present in leaves and how high resolution spatial and temporal imaging can help to resolve the different contributions of these independent processes to leaf form and function.

The microRNA miR396, which represesses growth by inhibiting GRFs, has been shown to be present in basipetal, acropetal and uniform patterns along the proximal-distal axes of different plant species (Das Gupta and Nath, 2015). It would be interesting if the growth patterns we measured had corollaries in species where the miR396 pattern is flipped from Arabidopsis, or is uniform. We predict in these cases, the juxtaposition of aligned growth patterns would switch proximal-distal locations or become medial-lateral in the case of uniform growth. As our study highlights, future work on these regulatory modules should focus on the generation of juxtaposed growth patterns in early leaf shaping.

Materials and Methods

Plant Growth Conditions

Live imaged plants were surface sterilized by washing once with 70% EtOH, 0.05% SDS solution for 7-10 minutes on a nutating shaker, then 3 subsequent washes with 100% EtOH, then dried on autoclaved filter paper. Seeds were sown on 0.5x Murashige and Skoog media (pH 5.7, 0.5 g/L MES, 1% phytoagar) supplemented with 1% sucrose. Plants grown to maturity were

grown on Lambert Mix LM-111 soil. All plants were stratified for at least 2 days at 4°C then transferred to Percival growth chambers and grown under 24-hour light, ~100 µmol m^{-2} s^{-1} at 22°C.

Plant accessions

WT plants are ecotype Col-0. *jaw-D* leaves are the *jaw-1D* allele from (Palatnik et al., 2003). Plants were crossed with the epidermal specific fluorescent reporters for plasma membrane (pAR169 *AtML1:mCitrine-RCI2a*) and nucleus (pAR229 *AtML1:H2B-TFP*) (Robinson et al., 2018; Roeder et al., 2010). Note, only the plasma membrane marker was imaged for the purposes of this paper. In subsequent generations, plants homozygous for both markers were selected.

Sample preparation – live imaging

Seedling germination times have inherent variability (Abley et al., 2021). In our hands, we found that the first two leaves of WT and *jaw-D* plants initiated three days after being exposed to our growth conditions (reported as Days After Sowing - DAS). At this stage, the cotyledons are fully greened and have bent at 90° angles from the stem. Therefore, we dissected cotyledons off the early seedlings 2 DAS, allowed the plants to rest for one day and then proceeded to capture images of growing first leaves using lines expressing the plasma membrane marker. Coverslips were suspended a few millimeters above the sample with vacuum grease to encourage leaves to remain in good imaging positions. Samples beneath coverslips were submerged in perfluorodecalin, a high refractive index compound that allows for proper gas exchange during imaging. More detail about our imaging method can be found in our recent publication (Harline and Roeder 2022).

Confocal imaging

Plants were imaged on a Zeiss 710 upright laser scanning confocal microscope with 20x Plan-Apochromat NA 1.0 water immersion lens, with z step between 0.5um and 1.0um. The plasma membrane mCitrine marker was excited with a 514 nm wavelength laser at 1-2% power and the emission spectra from 519-650nm was collected through a 458/514 filter. As samples grew and were too large to image in one stack, separate scans were taken and stacks manually aligned

and merged in MorphoGraphX 2.0 (Strauss et al., 2021).

Fully grown leaf imaging

First and second leaves were harvested from plants once fully grown, at least 31 DAS, and scanned with a Canon CanoScan LiDE 110 scanner.

Image processing – live imaging

Zeiss .LSM imaging files were converted to .TIF in ImageJ. Tiff files were imported into MorphoGraphX 2.0 (Strauss et al., 2021). The task list of MorphoGraphX processes used to create 2.5D representations of the confocal stacks are enclosed as Supplemental Information. Briefly, masks were created of the confocal stacks through 1-3 rounds of Gaussian blurring, then edge detection, closing holes in older samples where masks showed gaps, surface creation, manual selection and deletion of the surface that did not contain confocal signal and then projection of the confocal signal onto the surface. Meshes were subdivided once, then subject to 2-3 rounds of auto-segmentation, adaptive mesh subdivision at the new cell borders and projection of the confocal signal back onto the refined mesh. Cell segmentations were manually corrected immediately after segmentation or through the process of manual cell lineage tracing and cell junction correction using the check correspondence process. Cell and growth parameters were measured and heat maps generated using a python script run through MorphoGraphX 2.0. All >77,000 cells in the final analysis were selected based on the presence of lineage tracking ensuring that only cells that were manually curated were included in the final dataset. All segmented meshes and measures are included in Supplemental Data.

Image processing - fully grown leaves

Scanned leaf images were processed using the ROI tool in ImageJ. Each leaf was first outlined with the white paintbrush tool to color over bits of dirt and shadows. Images were then converted to 8-bit grayscale and a threshold of 187 was applied. To measure leaf area, each leaf outline was selected with the wand tool, filled in using the Ctrl+F shortcut and measured with the Ctrl+M shortcut. The whole leaf and lamina length were measured using the segmented line tool by tracing a line from tip to base of the lamina and then along the middle of the petiole. The lamina was

then digitally separated from the petiole by drawing over the petiole neck with the paintbrush tool. The separated lamina was selected with the wand tool and area measured with Ctrl+M. Petiole length and area were determined by subtracting the measured lamina values from the whole leaf values. Ripples were counted as protrusions visible in the thresholded images that were symmetrical along the proximal-distal axis (see Supplemental Figure 1I). Bulges on one side were counted as half ripples.

Data analysis

All data processing, analysis and plotting was performed in RStudio (2020; 2021). Sigmoidal models were fit using (Ritz et al., 2015). CVs were compared using (Ben Marwick and Kalimuthu Krishnamoorthy, 2019). Scripts used to process the data and create each figure can be found at https://github.com/kateharline/jawd-paper. We have provided the segmented meshes, measures of cellular growth, divisions and characteristics to enable further exploration into the variety of cell lineages we captured in this data set in Supplemental Data.

One dimensional model of leaf length

We developed a simple one-dimensional model to capture the length of the leaf over time. Our goal was to explore how contrasting spatial growth profiles for WT and *jaw-D* genotypes can lead to overall similar leaf length dynamics. These differences are clearly seen in Figure 4B on 4-6 DAS, where cell growth shows a sharp decline with the proximal-distal location in WT. In contrast, the spatial growth profiles are relatively flat with respect to the spatial position in *jaw-D*.

We formulate a discrete-time model where time $t = 0, 1, 2, \cdots$ corresponds to days and L_t is the leaf length at t days after sowing We assume that cells are arranged linearly in a one-dimensional lattice from position $i = 1, 2, \cdots L_t$. Let $\rho_{i,t}$ denote the probability of division for a cell at location i in time step t to $t + 1$. Then, the leaf length at time $t + 1$ is given by

$$L_{t+1} = Round\left[\sum_{i=1}^{L_t} 1 + \rho_{i,t}\right]$$

where $Round[\quad]$ is the nearest-integer operation. In this model, the probability $\rho_{i,t}$ is analogous

to the cellular growth rate. Starting from a single cell at position $i = 1$ at time $t = 0$, the length grows exponentially in the beginning. This is captured by having $\rho_{i,t} = 1$ as long as the leaf length L_t is below a threshold $\bar{L}$. As the leaf exits this initial exponential phase, $\rho_{i,t}$ becomes a function of both time/spatial location and also becomes different between WT and jaw-D.

For WT we consider the following functional form

$$\rho_{i,t} = \frac{\rho_{0,t}}{1 + (k\ i)^2}$$

that decreases with increasing distance from the leaf base i and k is a positive constant. Here $\rho_{0,t}$ is the growth at the leaf base which decreases over time, and this decrease is essential to eventually stop all growth as the leaf length approaches its steady-state value L_∞. We consider the following form for the growth rate at the leaf base that decreases with increasing length L_t

$$\rho_{0,t} = \frac{\left(1-\frac{L_t}{L_\infty}\right)^2}{\left(1-\frac{\bar{L}}{L_\infty}\right)^2}.$$

Given the flat growth profile seen in *jaw-D*, the probability of cell division is assumed to be independent of i and given by

$$\rho_{i,t} = \frac{\left(1-\frac{L_t}{L_\infty}\right)^2}{2\left(1-\frac{\bar{L}}{L_\infty}\right)^2}.$$

The model simulations are shown in the figure below with $\bar{L} = 50\ a.u.$, $L_\infty = 500\ a.u$, $k = 0.01$, and show similar length dynamics between the two genotypes

Analysis of Local Temporal and Spatial variability in Cell Growth

To quantify local temporal and spatial variability in cell growth we follow (Hong et al., 2016). The areal growth rate of a cell between two consecutive time points is defined by $AGR_1 = (A_1/A_2)/t$, where A_1 and A_2 denote the cell area in the first and second time point, respectively, and t is the elapsed time between the time points measured in hours. If the cell has divided between the two time points A_2 is the sum of the areas of all daughter cells. Local temporal variability in cell area growth is measured using the formula $D_{area} = |AGR_1 - AGR_2| / |AGR_1 + AGR_2|$. Since this measure is calculated based on 3 consecutive time points it is ambiguous for which time point we are measuring temporal variability. To resolve this ambiguity we always use the formula to measure

the temporal variability at the second (middle) time point. Given a cell c the local spatial variability of the cell is measured using its areal growth rate AGR(c) and the areal growth rates of its bordering neighbors AGR(i), i = 1,2,...,k, where k denotes the number of bordering neighbors. Local spatial variability in cell area growth is measured using the formula $V_{area} = \sum_{i=1}^{k} | AGR(c) - AGR(i) | / | AGR(c) + AGR(i) |$. The local spatial variability is only calculated based on two time points and the formula is used to measure the variability at the first time point.

Cellular Fourier analysis

Below we summarize the main steps of the spectral analysis. For more technical details, refer to supplementary information and (Fruleux and Boudaoud 2021).

We analyze the areal growth rate and the deformation of tissues. The areal growth rate of each cell is defined as the relative difference of their surface areas at successive time steps divided by the time delay between two time steps. The deformation is a symmetric matrix summarizing the two principal directions of growth, and the ratios to apply in these two directions to deform a cell's contour at a preceding time step to the same cell's contour at a following time step.

We then perform the spectral analysis consisting by representing the spatial variation of the areal growth or of the deformation matrix as a linear combination of harmonics. Each harmonic is associated to a frequency characterizing its spatial variation scale. Performing our analysis we obtain the Cellular Fourier Transforms of the areal growth rate and of the deformation. These are the amplitudes with which the different harmonics decompose the areal growth rate and the deformation matrix. For a tissue, the first harmonic is a constant associated to the spatial frequency 0, and the corresponding CFT for the areal growth rate is the whole tissue's areal growth. The two following harmonics vary at the scale of the tissue and the associated CFTs for the areal growth rate give the average growth gradient at the tissue scale. The higher the rank of the harmonics is, the higher the spatial frequency and the smaller the considered space scale are. The deformation being described by a matrix, its CFTs are also matrices. The first CFT will for example be the average tissue deformation. We notice that, although a cell's deformation is 2D and contained in its tangential plane, if it is not flat, the overall tissue deforms in 3D. The CFTs of the

deformation matrix depend therefore on the tissue geometry. To analyze growth anisotropy, we considered the difference between the two first eigenvalues of the CFTs of deformation which we divided by the time delay between two time steps. It quantifies the deviation from isotropic deformation.

The spectra we finally considered are those of the areal growth rate and the deviation from isotropic growth. These spectra have been smoothed to be comparable among different tissues. In these spectra the y-axis represent the CFTs and the x-axis spatial frequencies. Low frequencies correspond to large spatial variation scales and high frequencies to small spatial variation scales. Space frequencies equal to one correspond to the cell scale (mean cell size).

Finite element method simulations

The template for the growing leaf model was created from an initial contour representing the young leaf shape. This was triangulated and then extruded into a sheet made of a single layer of wedges (prisms). This follows the structure of previous models of leaf shape (Kuchen et al., 2012), although in our model a small amount of noise was added to the vertices in the normal direction allowing the structure to bend out of the plane. The MorphoMechanX (www.MorphoMechanX.org) modeling framework was used for the FEM simulation (Bassel et al., 2014; Mosca et al., 2017; Natonik-Białoń et al., 2020). An isotropic linear material model was used. Growth was implemented by increasing the size of the reference configuration of the elements, with independent control of growth parallel or perpendicular to a growth axis. The rates of growth and the growth direction were specified manually based on qualitative assessment of live imaging data. After each growth step, the mechanical equilibrium was found, and residual stresses were released. Any wedges above a threshold volume were subdivided, and values for growth parameters were reassigned. The simulation models are enclosed as Supplemental Information.

Acknowledgements

The authors would like to *thank* the Roeder, Scanlon, Boudaoud, Hamant and Smith labs for helpful d**iscussio**ns and advice on the manuscript. We thank Javier Palatnik for information on the jaw-D insertion site. We thank Zahava Rojer for technical assistance.

Funding

This work was funded by an NSF Graduate Research Fellowship (NSF Graduate Research Fellowship (DGE-1650441) to K.H., NSF MCB-2203275; The Schwartz Research Fund Award and National Institute Of General Medical Sciences of the National Institutes of Health under Award Number R01GM134037 to A.H.K.R.; Agence Nationale de la Recherche (FR) Grant# ANR-21-CE30-0039-01 to A.B.; Institute Strategic Program Grant from the BBSRC to the John Innes Centre (BB/P013511/1) to R.S.S. and B.L.; Deutsche Forschungsgemeinschaft (FOR2581) to S.S. and G.M.; NSF Grant ECCS-1711548 to A.S.; Investissements d'Avenir du LabEx PALM (ANR-10-LABX-0039-PALM) to A.F. and paired PhD programme of the Faculty of Science, Stockholm University [SU FV-1.2.1-0124-17) to C-B.L. and N.T. The content is solely the responsibility of the authors and does not necessarily represent the official views of the National Institutes of Health.

Author Contributions

K.H., J.W.S. and A.H.K.R conceived experiments. K.H. conducted live imaging experiments, image processing, cell growth and characteristics data analysis. K.H., A.H.K.R., A.F. A.B., N.K., C-B.L., R.S.S. conceived analyses. A.F. conducted cellular fourier analysis. N.K. conducted spatio-temporal analysis. B.L. and A.S. conducted leaf growth modeling. S.S., R.S.S. and G.M. developed and provided support for MorphoGraphX. K.H. and A.H.K.R. wrote the manuscript and assembled figures. All authors contributed to manuscript preparation and editing.

REFERENCES

Abley, K., Formosa-Jordan, P., Tavares, H., Chan, E.Y., Afsharinafar, M., Leyser, O., and Locke, J.C. (2021). An ABA-GA bistable switch can account for natural variation in the variability of Arabidopsis seed germination time. eLife **10**.

Alvarez, J.P., Furumizu, C., Efroni, I., Eshed, Y., and Bowman, J.L. (2016). Active suppression of a leaf meristem orchestrates determinate leaf growth. eLife **5**.

Armon, S., Moshe, M., and Sharon, E. (2021). The multiscale nature of leaf growth fields. Commun. Phys. **4**: 122.

Avery, G.S. (1933). Structure and development of the tobacco leaf. Am. J. Bot. **20**: 565.

Bassel, G.W., Stamm, P., Mosca, G., Barbier de Reuille, P., Gibbs, D.J., Winter, R., Janka, A., Holdsworth, M.J., and Smith, R.S. (2014). Mechanical constraints imposed by 3D cellular geometry and arrangement modulate growth patterns in the *Arabidopsis* embryo. Proc Natl Acad Sci USA **111**: 8685–8690.

Beltramino, M., Ercoli, M.F., Debernardi, J.M., Goldy, C., Rojas, A.M.L., Nota, F., Alvarez, M.E., Vercruyssen, L., Inzé, D., Palatnik, J.F., and Rodriguez, R.E. (2018). Robust increase of leaf size by Arabidopsis thaliana GRF3-like transcription factors under different growth conditions. Sci. Rep. **8**: 13447.

Ben Amar, M. and Jia, F. (2013). Anisotropic growth shapes intestinal tissues during embryogenesis. Proc Natl Acad Sci USA **110**: 10525–10530.

Ben Marwick and Kalimuthu Krishnamoorthy (2019). Testing Coefficients of Variation from multiple samples.

Blein, T., Pautot, V., and Laufs, P. (2013). Combinations of Mutations Sufficient to Alter Arabidopsis Leaf Dissection. Plants **2**: 230–247.

Boudaoud, A. (2010). An introduction to the mechanics of morphogenesis for plant biologists. Trends Plant Sci. **15**: 353–360.

Bresso, E.G., Chorostecki, U., Rodriguez, R.E., Palatnik, J.F., and Schommer, C. (2018). Spatial Control of Gene Expression by miR319-Regulated TCP Transcription Factors in Leaf Development. Plant Physiol. **176**: 1694–1708.

Caggiano, M.P., Yu, X., Bhatia, N., Larsson, A., Ram, H., Ohno, C.K., Sappl, P., Meyerowitz, E.M., Jönsson, H., and Heisler, M.G. (2017). Cell type boundaries organize plant development. eLife **6**.

Challa, K.R., Rath, M., and Nath, U. (2019). The CIN-TCP transcription factors promote commitment to differentiation in Arabidopsis leaf pavement cells via both auxin-dependent and independent pathways. PLoS Genet. **15**: e1007988.

Challa, K.R., Rath, M., Sharma, A.N., Bajpai, A.K., Davuluri, S., Acharya, K.K., and Nath, U. (2021). Active suppression of leaflet emergence as a mechanism of simple leaf development. Nat. Plants **7**: 1264–1275.

Chuck, G., Lincoln, C., and Hake, S. (1996). KNAT1 induces lobed leaves with ectopic meri-

stems when overexpressed in Arabidopsis. Plant Cell **8**: 1277–1289.

Coen, E. and Rebocho, A.B. (2016). Resolving conflicts: modeling genetic control of plant morphogenesis. Dev. Cell **38**: 579–583.

Crawford, B.C.W., Nath, U., Carpenter, R., and Coen, E.S. (2004). CINCINNATA controls both cell differentiation and growth in petal lobes and leaves of Antirrhinum. Plant Physiol. **135**: 244–253.

Das Gupta, M. and Nath, U. (2015). Divergence in Patterns of Leaf Growth Polarity Is Associated with the Expression Divergence of miR396. Plant Cell **27**: 2785–2799.

Debernardi, J.M., Mecchia, M.A., Vercruyssen, L., Smaczniak, C., Kaufmann, K., Inze, D., Rodriguez, R.E., and Palatnik, J.F. (2014). Post-transcriptional control of GRF transcription factors by microRNA miR396 and GIF co-activator affects leaf size and longevity. Plant J. **79**: 413–426.

Debernardi, J.M., Rodriguez, R.E., Mecchia, M.A., and Palatnik, J.F. (2012). Functional specialization of the plant miR396 regulatory network through distinct microRNA-target interactions. PLoS Genet. **8**: e1002419.

Derr, J., Bastien, R., Couturier, É., and Douady, S. (2018). Fluttering of growing leaves as a way to reach flatness: experimental evidence on Persea americana. J. R. Soc. Interface **15**.

Donnelly, P.M., Bonetta, D., Tsukaya, H., Dengler, R.E., and Dengler, N.G. (1999). Cell cycling and cell enlargement in developing leaves of Arabidopsis. Dev. Biol. **215**: 407–419.

Efroni, I., Blum, E., Goldshmidt, A., and Eshed, Y. (2008). A protracted and dynamic maturation schedule underlies Arabidopsis leaf development. Plant Cell **20**: 2293–2306.

Fox, S. et al. (2018). Spatiotemporal coordination of cell division and growth during organ morphogenesis. PLoS Biol. **16**: e2005952.

Fruleux, A. and Boudaoud, A. (2021). Cellular Fourier analysis for geometrically disordered materials. Phys. Rev. Research **3**: 023036.

Hamant, O., Heisler, M.G., Jönsson, H., Krupinski, P., Uyttewaal, M., Bokov, P., Corson, F., Sahlin, P., Boudaoud, A., Meyerowitz, E.M., Couder, Y., and Traas, J. (2008). Developmental patterning by mechanical signals in Arabidopsis. Science **322**: 1650–1655.

Hannezo, E., Prost, J., and Joanny, J.F. (2011). Instabilities of monolayered epithelia: shape and structure of villi and crypts. Phys. Rev. Lett. **107**: 078104.

Harline, K. and Roeder, A.H.K. (2022). An optimized pipeline for live imaging whole Arabidopsis leaves at cellular resolution. BioRxiv. 10.1101/2022.11.01.514724

Hong, L. et al. (2016). Variable Cell Growth Yields Reproducible OrganDevelopment through Spatiotemporal Averaging. Dev. Cell **38**: 15–32.

Karzbrun, E., Kshirsagar, A., Cohen, S.R., Hanna, J.H., and Reiner, O. (2018). Human brain organoids on a chip reveal the physics of folding. Nat. Phys. **14**: 515–522.

Kazama, T., Ichihashi, Y., Murata, S., and Tsukaya, H. (2010). The mechanism of cell cycle arrest front progression explained by a KLUH/CYP78A5-dependent mobile growth factor in developing leaves of Arabidopsis thaliana. Plant Cell Physiol. **51**: 1046–1054.

Kierzkowski, D. et al. (2019). A Growth-Based Framework for Leaf Shape Development and Diversity. Cell **177**: 1405-1418.e17.

Koehl, M.A.R., Silk, W.K., Liang, H., and Mahadevan, L. (2008). How kelp produce blade shapes suited to different flow regimes: A new wrinkle. Integr. Comp. Biol. **48**: 834–851.

Koyama, T., Furutani, M., Tasaka, M., and Ohme-Takagi, M. (2007). TCP transcription factors control the morphology of shoot lateral organs via negative regulation of the expression of boundary-specific genes in Arabidopsis. Plant Cell **19**: 473–484.

Koyama, T., Mitsuda, N., Seki, M., Shinozaki, K., and Ohme-Takagi, M. (2010). TCP transcription factors regulate the activities of ASYMMETRIC LEAVES1 and miR164, as well as the auxin response, during differentiation of leaves in Arabidopsis. Plant Cell **22**: 3574–3588.

Koyama, T., Sato, F., and Ohme-Takagi, M. (2017). Roles of miR319 and TCP Transcription Factors in Leaf Development. Plant Physiol. **175**: 874–885.

Kuchen, E.E., Fox, S., de Reuille, P.B., Kennaway, R., Bensmihen, S., Avondo, J., Calder, G.M., Southam, P., Robinson, S., Bangham, A., and Coen, E. (2012). Generation of leaf shape through early patterns of growth and tissue polarity. Science **335**: 1092–1096.

Le Gloanec, C., Collet, L., Silveira, S.R., Wang, B., Routier-Kierzkowska, A.-L., and Kierzkowski, D. (2022). Cell type-specific dynamics underlie cellular growth variability in plants. Development **149**.

Marder, M., Sharon, E., Smith, S., and Roman, B. (2003). Theory of edges of leaves. Europhys. Lett. **62**: 498–504.

Mosca, G., Sapala, A., Strauss, S., Routier-Kierzkowska, A.-L., and Smith, R.S. (2017). On

the micro-indentation of plant cells in a tissue context. Phys. Biol. **14**: 015003.

al-Mosleh, S. and Mahadevan, L. (2022). How to grow a flat leaf. arXiv.

Nag, A., King, S., and Jack, T. (2009). miR319a targeting of < em>TCP4< /em> is critical for petal growth and development in < em>Arabidopsis< /em>. Proceedings of the National Academy of Sciences **106**: 22534 LP – 22539.

Nakata, M., Matsumoto, N., Tsugeki, R., Rikirsch, E., Laux, T., and Okada, K. (2012). Roles of the middle domain-specific WUSCHEL-RELATED HOMEOBOX genes in early development of leaves in Arabidopsis. Plant Cell **24**: 519–535.

Nath, U., Crawford, B.C.W., Carpenter, R., and Coen, E. (2003). Genetic control of surface curvature. Science **299**: 1404–1407.

Natonik-Białoń, S., Borowska-Wykręt, D., Mosca, G., Grelowski, M., Wrzalik, R., Smith, R.S., and Kwiatkowska, D. (2020). Deformation of a cell monolayer due to osmotic treatment: a case study of onion scale epidermis. Botany **98**: 21–36.

Nelson, C.M. (2016). On Buckling Morphogenesis. J. Biomech. Eng. **138**: 021005.

Ori, N. et al. (2007). Regulation of LANCEOLATE by miR319 is required for compound-leaf development in tomato. Nat. Genet. **39**: 787–791.

Palatnik, J.F., Allen, E., Wu, X., Schommer, C., Schwab, R., Carrington, J.C., and Weigel, D. (2003). Control of leaf morphogenesis by microRNAs. Nature **425**: 257–263.

Palatnik, J.F., Wollmann, H., Schommer, C., Schwab, R., Boisbouvier, J., Rodriguez, R., Warthmann, N., Allen, E., Dezulian, T., Huson, D., Carrington, J.C., and Weigel, D. (2007). Sequence and expression differences underlie functional specialization of Arabidopsis microRNAs miR159 and miR319. Dev. Cell **13**: 115–125.

Poethig, R.S. and Sussex, I.M. (1985). The developmental morphology and growth dynamics of the tobacco leaf. Planta **165**: 158–169.

Rebocho, A.B., Southam, P., Kennaway, J.R., Bangham, J.A., and Coen, E. (2017). Generation of shape complexity through tissue conflict resolution. eLife **6**.

Reinhardt, D., Pesce, E.-R., Stieger, P., Mandel, T., Baltensperger, K., Bennett, M., Traas, J., Friml, J., and Kuhlemeier, C. (2003). Regulation of phyllotaxis by polar auxin transport. Nature **426**: 255–260.

Remmler, L. and Rolland-Lagan, A.-G. (2012). Computational method for quantifying growth

patterns at the adaxial leaf surface in three dimensions. Plant Physiol. **159**: 27–39.

Ritz, C., Baty, F., Streibig, J.C., and Gerhard, D. (2015). Dose-Response Analysis Using R. PLoS ONE **10**: e0146021.

Robinson, D.O., Coate, J.E., Singh, A., Hong, L., Bush, M., Doyle, J.J., and Roeder, A.H.K. (2018). Ploidy and size at multiple scales in the Arabidopsis sepal. Plant Cell **30**: 2308–2329.

Rodriguez, R.E., Debernardi, J.M., and Palatnik, J.F. (2014). Morphogenesis of simple leaves: regulation of leaf size and shape. Wiley Interdiscip. Rev. Dev. Biol. **3**: 41–57.

Rodriguez, R.E., Ercoli, M.F., Debernardi, J.M., Breakfield, N.W., Mecchia, M.A., Sabatini, M., Cools, T., De Veylder, L., Benfey, P.N., and Palatnik, J.F. (2015). MicroRNA miR396 Regulates the Switch between Stem Cells and Transit-Amplifying Cells in Arabidopsis Roots. Plant Cell **27**: 3354–3366.

Rodriguez, R.E., Mecchia, M.A., Debernardi, J.M., Schommer, C., Weigel, D., and Palatnik, J.F. (2010). Control of cell proliferation in Arabidopsis thaliana by microRNA miR396. Development **137**: 103–112.

Roeder, A.H.K., Chickarmane, V., Cunha, A., Obara, B., Manjunath, B.S., and Meyerowitz, E.M. (2010). Variability in the control of cell division underlies sepal epidermal patterning in Arabidopsis thaliana. PLoS Biol. **8**: e1000367.

RStudio Team (2020). RStudio. RStudio: Integrated Development for R.

Rubio-Somoza, I., Zhou, C.-M., Confraria, A., Martinho, C., von Born, P., Baena-Gonzalez, E., Wang, J.-W., and Weigel, D. (2014). Temporal control of leaf complexity by miRNA-regulated licensing of protein complexes. Curr. Biol. **24**: 2714–2719.

R Core Team (2021). R: The R Project for Statistical Computing.

Sapala, A. et al. (2018). Why plants make puzzle cells, and how their shape emerges. eLife **7**.

Sarojam, R., Sappl, P.G., Goldshmidt, A., Efroni, I., Floyd, S.K., Eshed, Y., and Bowman, J.L. (2010). Differentiating Arabidopsis shoots from leaves by combined YABBY activities. Plant Cell **22**: 2113–2130.

Sarvepalli, K. and Nath, U. (2011). Hyper-activation of the TCP4 transcription factor in Arabidopsis thaliana accelerates multiple aspects of plant maturation. Plant J. **67**: 595–607.

Sauret-Güeto, S., Schiessl, K., Bangham, A., Sablowski, R., and Coen, E. (2013). JAGGED controls Arabidopsis petal growth and shape by interacting with a divergent polarity field.

PLoS Biol. **11**: e1001550.

Schommer, C., Debernardi, J.M., Bresso, E.G., Rodriguez, R.E., and Palatnik, J.F. (2014). Repression of cell proliferation by miR319-regulated TCP4. Mol. Plant **7**: 1533–1544.

Schommer, C., Palatnik, J.F., Aggarwal, P., Chételat, A., Cubas, P., Farmer, E.E., Nath, U., and Weigel, D. (2008). Control of jasmonate biosynthesis and senescence by miR319 targets. PLoS Biol. **6**: e230.

Sharon, E., Roman, B., Marder, M., Shin, G.-S., and Swinney, H.L. (2002). Mechanics. Buckling cascades in free sheets. Nature **419**: 579.

Shyer, A.E., Tallinen, T., Nerurkar, N.L., Wei, Z., Gil, E.S., Kaplan, D.L., Tabin, C.J., and Mahadevan, L. (2013). Villification: how the gut gets its villi. Science **342**: 212–218.

Skopelitis, D.S., Husbands, A.Y., and Timmermans, M.C.P. (2012). Plant small RNAs as morphogens. Curr. Opin. Cell Biol. **24**: 217–224.

Strauss, S. et al. (2022). Using positional information to provide context for biological image analysis with MorphoGraphX 2.0. eLife **11**.

Sun, X., Wang, C., Xiang, N., Li, X., Yang, S., Du, J., Yang, Y., and Yang, Y. (2017). Activation of secondary cell wall biosynthesis by miR319-targeted TCP4 transcription factor. Plant Biotechnol. J. **15**: 1284–1294.

Tallinen, T., Chung, J.Y., Rousseau, F., Girard, N., Lefèvre, J., and Mahadevan, L. (2016). On the growth and form of cortical convolutions. Nat. Phys. **12**: 588–593.

Tozluoğlu, M., Duda, M., Kirkland, N.J., Barrientos, R., Burden, J.J., Muñoz, J.J., and Mao, Y. (2019). Planar differential growth rates initiate precise fold positions in complex epithelia. Dev. Cell **51**: 299-312.e4.

Traas, J. and Doonan, J.H. (2001). Cellular basis of shoot apical meristem development. In International review of cytology. (Elsevier), pp. 161–206.

Tsuge, T., Tsukaya, H., and Uchimiya, H. (1996). Two independent and polarized processes of cell elongation regulate leaf blade expansion in Arabidopsis thaliana (L.) Heynh. Development **122**: 1589–1600.

Warthmann, N., Das, S., Lanz, C., and Weigel, D. (2008). Comparative analysis of the MIR319a microRNA locus in Arabidopsis and related Brassicaceae. Mol. Biol. Evol. **25**: 892–902.

Weigel, D. et al. (2000). Activation tagging in Arabidopsis. Plant Physiol. **122**: 1003–1013.

Zhang, Z., Runions, A., Mentink, R.A., Kierzkowski, D., Karady, M., Hashemi, B., Huijser, P., Strauss, S., Gan, X., Ljung, K., and Tsiantis, M. (2020). A WOX/auxin biosynthesis module controls growth to shape leaf form. Curr. Biol.

Zhao, F. et al. (2020). Microtubule-Mediated Wall Anisotropy Contributes to Leaf Blade Flattening. Curr. Biol. **30**: 3972-3985.e6.

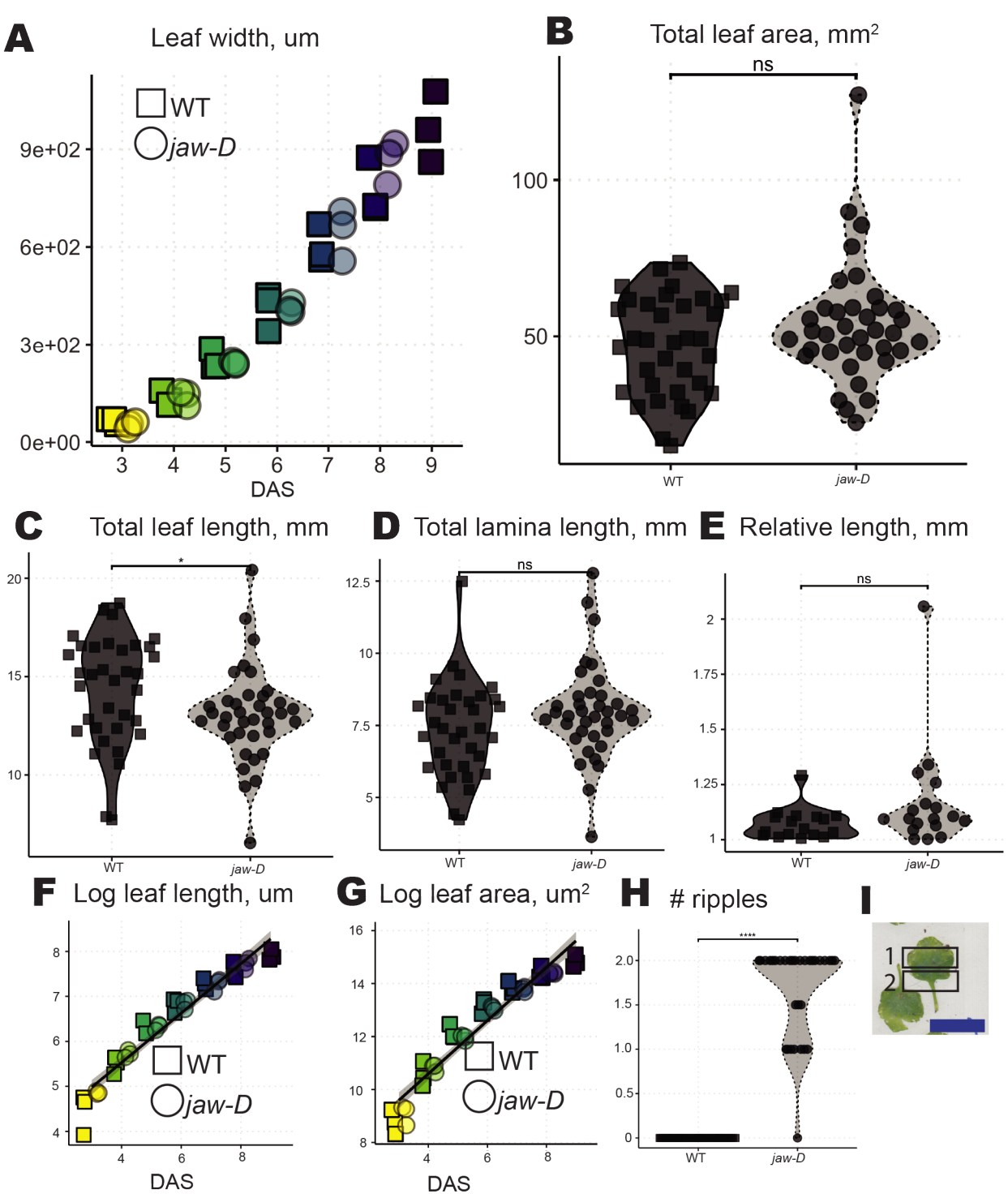

Supplemental Figure 1. | Additional features of live imaged and fully grown leaves. (A) Leaf width increases exponentially in WT (squares) and *jaw-D* (circles) leaves during the live imaging experiment. Colors indicate DAS. (B) Final leaf area of fully grown first and second leaves between WT and *jaw-D* is not significantly different, though the distributions are distinct with

WT showing a bimodal distribution and *jaw-D* with a more common median value and more extreme values. (B-E) Color, shape and linetype indicate genotype (solid, squares, dark gray = WT; dotted, circles, light gray = *jaw-D*) (C) Total leaf length of fully grown first and second leaves between WT and *jaw-D* shows a similar pattern with slightly shorter leaves in *jaw-D,* likely due to petiole length differences only ($p < 0.05$, Wilcox test). (D) Median length of the lamina measured from the petiole insertion point to the distal tip of the leaf is not significantly different between fully grown WT and *jaw-D* leaves ($p > 0.05$, Wilcox test). (E) The median relative length between the first and second leaves within the same plants of WT and *jaw-D* is not significantly different, though *jaw-D* exhibits much more extreme values ($p > 0.05$ Wilcox test). (F-G) The logarithm of leaf length (F) and leaf area (G) with plotting as in (A) demonstrate these values are increasing exponentially over the live imaging experiment. (H) Number of ripples per leaf in first two leaves of WT or *jaw-D* plotting as in B-E. (I) Example designation and counting of ripples. Blue scale bar = 10mm.

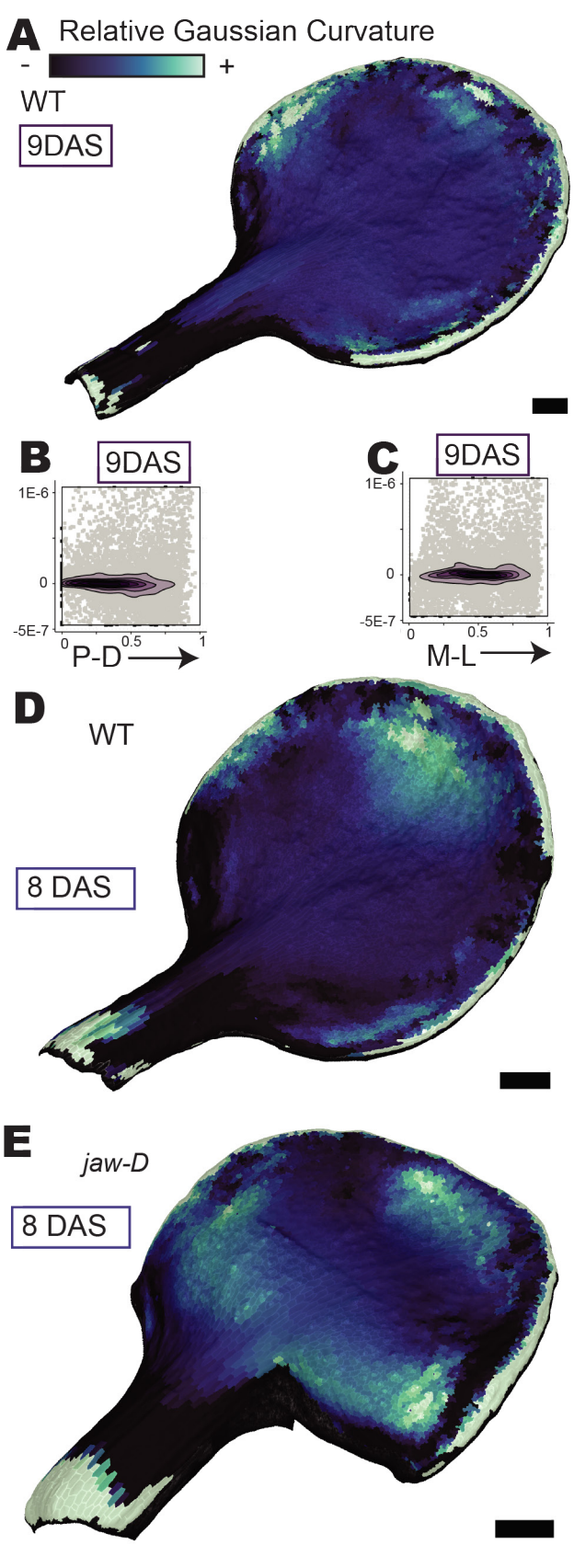

Supplemental Figure 2. | Extended curvature data (A) Relative curvature represented as a heatmap on a 9 DAS WT leaf sample. Black bars = 200 µm. (B-C) Quantification for all three WT lamina replicates of curvature along the proximal-distal (B) and medial-lateral (C) axes for 9 DAS leaves. Position axes are normalized between 0 and 1 for a given lamina replicate at a given time point. (D) Larger sample heatmap of WT curvature at 8 DAS (E) Larger sample heatmap of *jaw-D* curvature at 8 DAS.

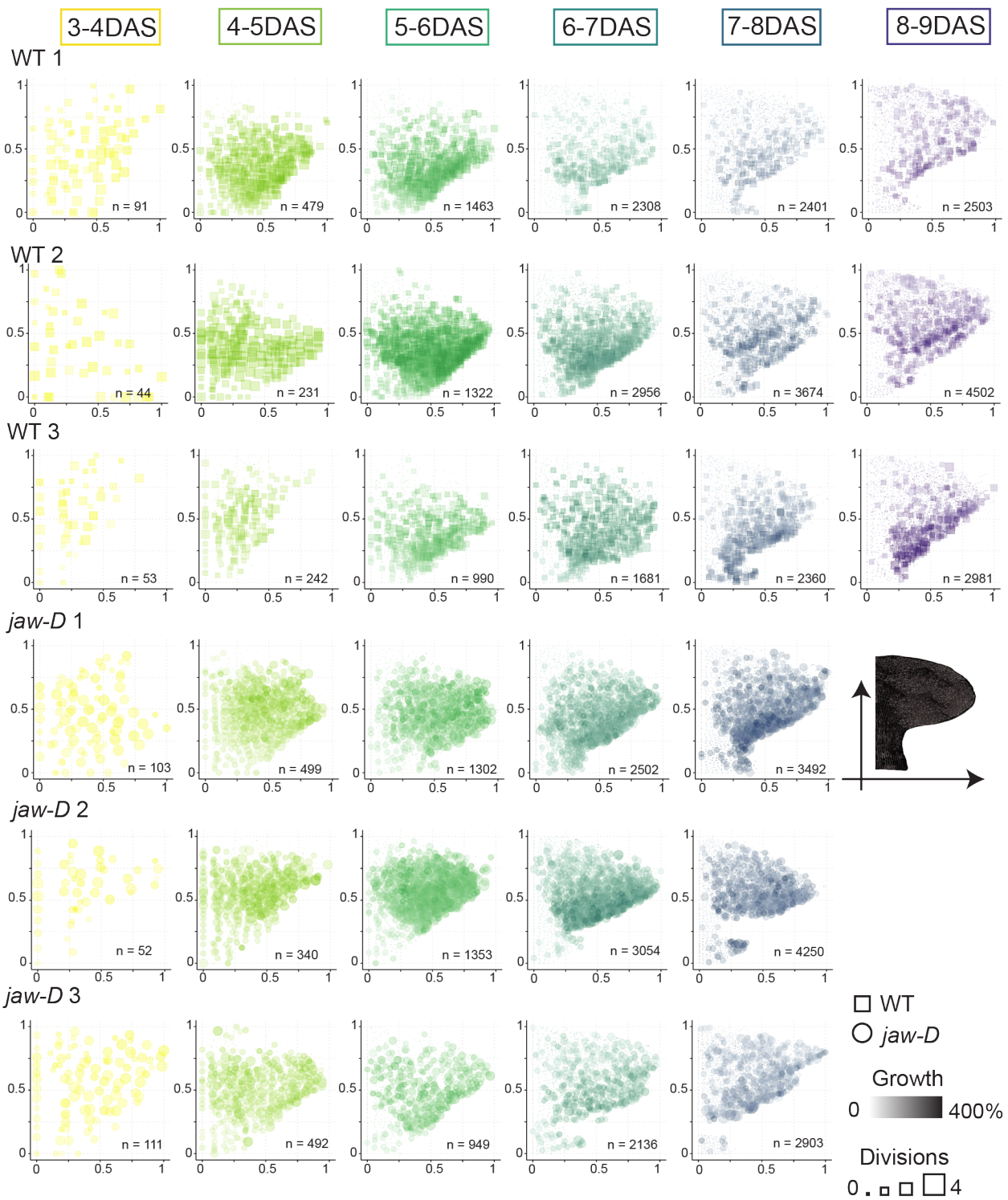

Supplemental Figure 3. | Growth and division patterns are consistent between replicates

Distribution of cell growth and division of each cell for one day intervals per whole leaf sample of WT (first three rows) and *jaw-D* (last three rows). N indicates the number of cells in each panel. The x and y axes represent medial-lateral and proximal-distal positions, respectively, normal-

ized between 0 and 1 for the given leaf and time point. Colors indicate 24 hour time points. The size and color intensity of each point represents the number of divisions and areal growth, respectively, a cell has experienced between imaging days. Note, in the main text Figure 3 the petiole and lamina lengths were calculated separately by selecting different ‘base cells’ to measure the distance from in MorphoGraphX. Normalization was performed on these separated measures. Panels in Supplemental Figure 3 do not separate cells between the petiole and the lamina so the proximal-distal normalization is from the base of the petiole

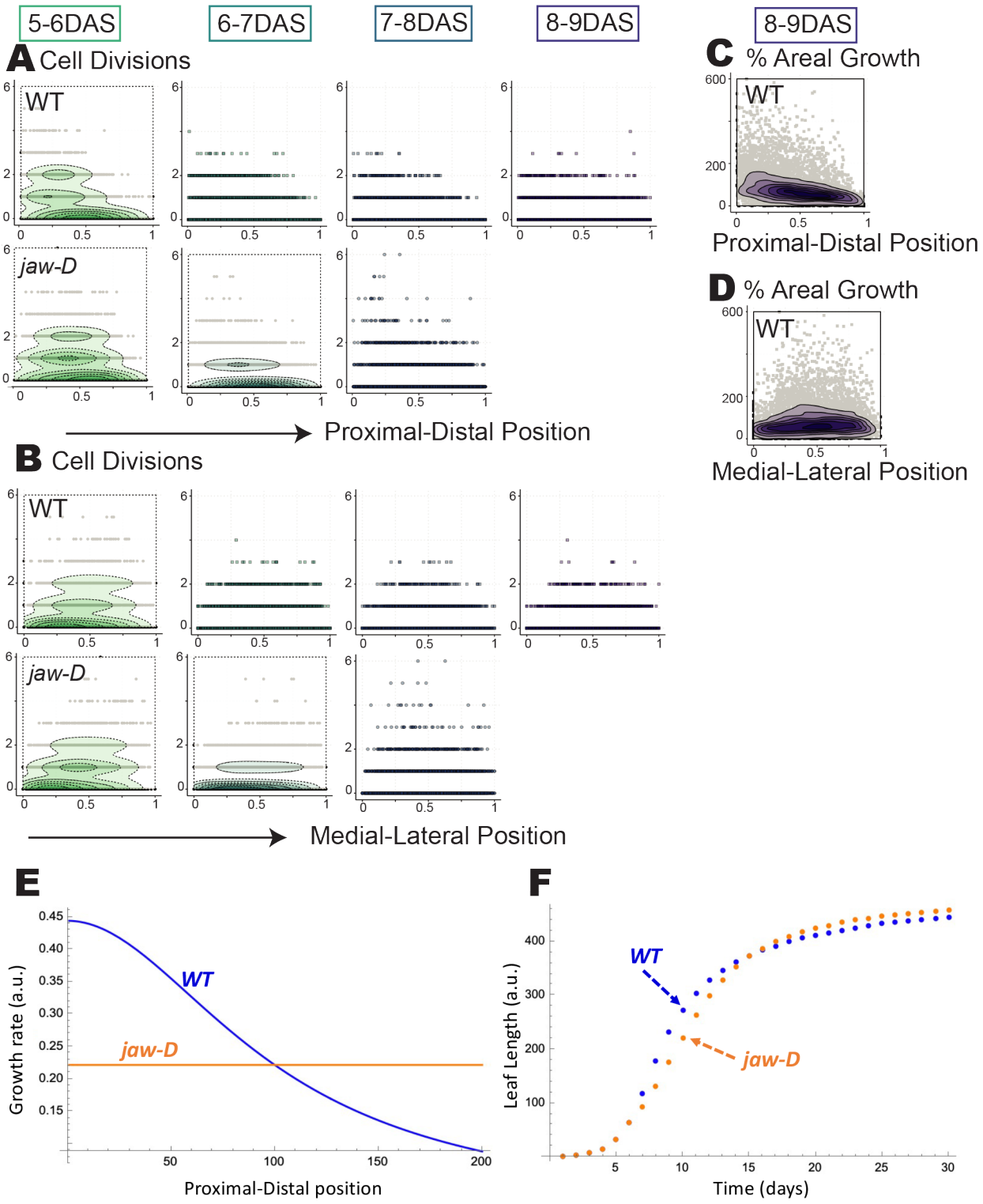

Supplemental Figure 4. | Later time point division patterns and leaf length model (A-B) Cell divisions over 24 hour intervals versus position along the proximal-distal axis (A) or medial-lateral axis (B) for each cell in all three WT (top, solid lines, squares) lamina replicates or

jaw-D (bottom, dotted lines, circles) replicates. Cell divisions are concentrated more distally in *jaw-D* than WT. Cell divisions are distributed more similarly between WT and *jaw-D* along the medial-lateral axis. (C-D) Areal growth from 8-9 DAS versus position along the proximal-distal axis (C) or medial-lateral axis (D) for each cell in all three WT (top, solid lines) lamina replicates. WT maintains a slight proximal maximum, but largely the leaf is growing through uniform expansion at this point. Use of density plots, coloring, axis selection and normalization as in Figure 4. Note, density plots in later time points were not calculated if the majority of cells were not dividing. In this case, only points representing individual cells are plotted. (E-F) Leaf length model with growth distribution across the leaf (E) and resultant leaf length (F) represented for WT (blue) and *jaw-D* (orange) simulated values.The growth rate profiles in (E) correspond to a leaf length of 200 a.u. in (F).

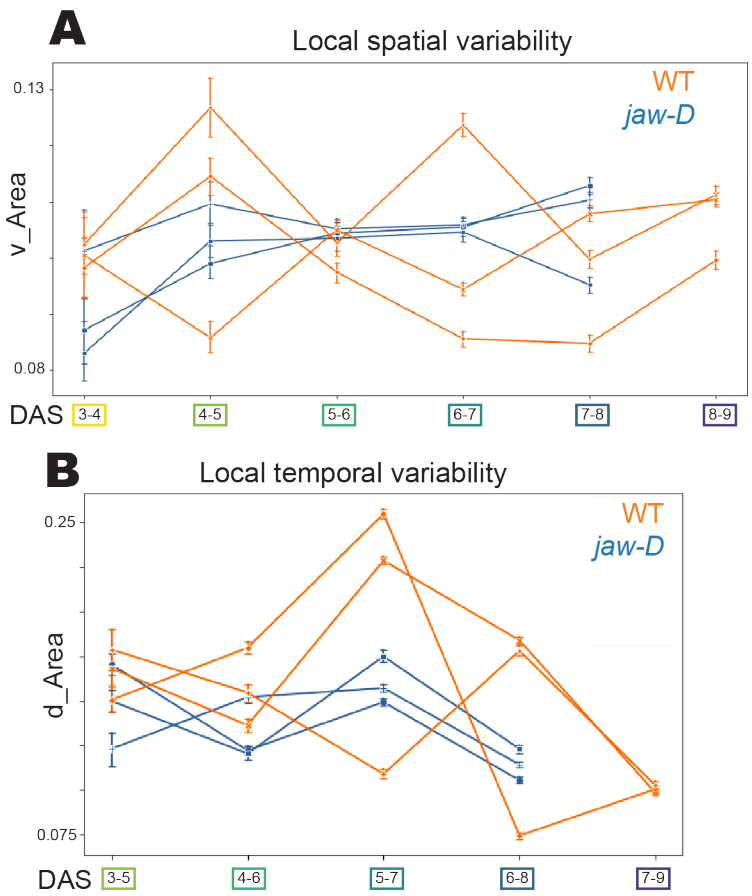

Supplemental Figure 5. | Spatio-temporal analysis with stomata excluded (A-B) Quantification of the mean (A) local growth spatial variability or (B) local growth temporal variability for time windows as in main Figure 3, with stomata excluded. Excluding stomata does not change patterns of growth heterogeneity observed between WT and *jaw-D*. WT and *jaw-D* local spatial and temporal growth variability are largely indistinguishable, though *jaw-D* replicates are generally tighter around the mean.

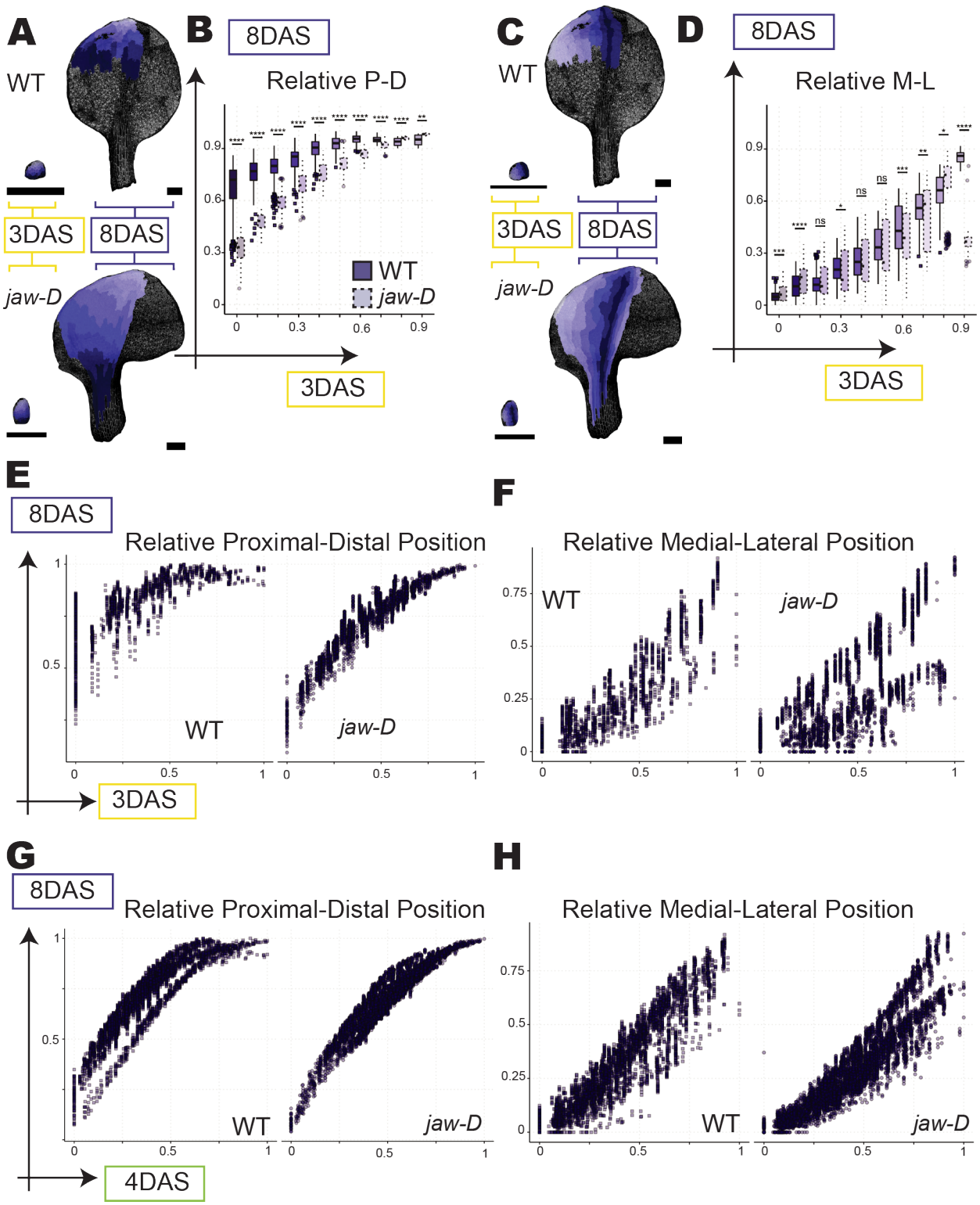

Supplemental Figure 6. | Additional clonal analysis

(A-D) Clonal analysis as in Figure 5, except in 3 DAS bins to 8 DAS locations. WT (top) and *jaw-D* (bottom) samples with ten clonal sectors from 3 DAS mapped onto the 8 DAS mesh in

shades of purple along the proximal-distal (A) or medial-lateral (C) axis. (B,D) Quantification for all three whole leaf replicates. WT (left, dark shading, solid lines) and *jaw-D* (right, light shading, dotted lines). Boxes indicate the 75% interquartile range, middle bar represents median, whiskers represent outliers and squares (WT) or circles (*jaw-D)* represent extreme values. Nearly all 3 DAS proximal-distal bins have similar to enhanced results as 4 DAS with significant differences for 8 DAS locations between WT and *jaw-D,* while medial-lateral contributions are more mixed (**** = p<.0001, ** = p <.01, * = p <.05, paired Student's t-test and Bonferroni correction). Final leaf contributions from WT seem to emerge mostly mid-leaf and a consistent stronger contribution from *jaw-D* lateral domains. Black scale bars = 200 µm. (E-H) Plots of all cells at 8 DAS versus their relative proximal-distal (E,G) or medial-lateral (F,H) position in the 3DAS (E-F) or 4DAS (G-H) leaf. Bifurcations in *jaw-D* medial-lateral positions could indicate tissue growth conflicts that induce rippling (F,H).

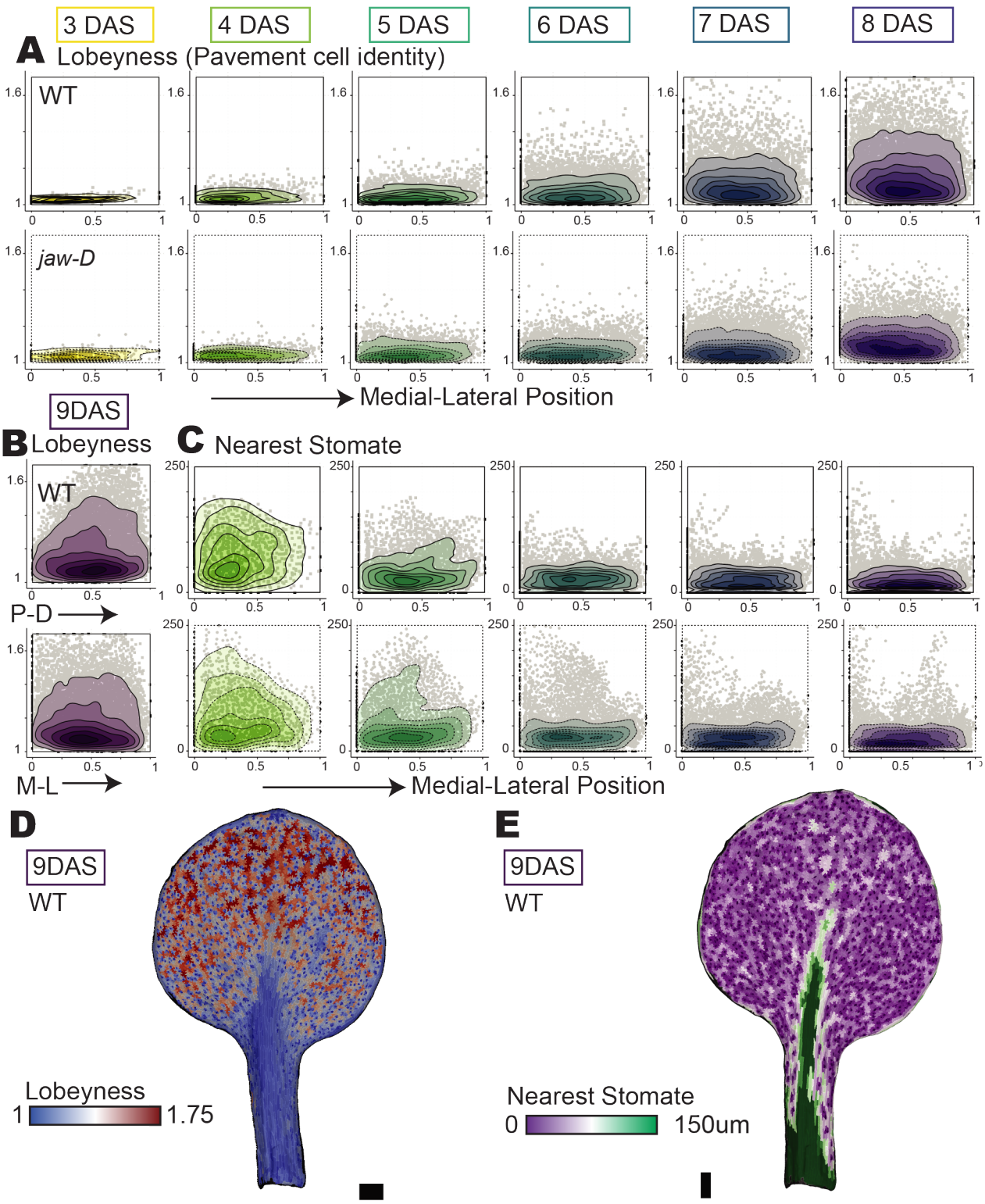

Supplemental Figure 7. | Additional differentiation quantification

(A-B) Lobeyness (the perimeter of a cell divided by its convex hull, a measure of pavement cell identity) versus position along the indicated axis for each cell in all three WT (top, squares, solid

lines) or *jaw-D* (bottom, circles, dotted lines) lamina replicates. Lobeyness is more evenly distributed across the medial-lateral axis in WT and *jaw-D* with greater absolute magnitude in WT. (C) Quantification of stomatal spacing (the distance in µm from pavement cells to the nearest stomata, the inverse of stomatal density) with plotting as in (A-B). Note, stomata first initiate at 4DAS. Stomatal spacing is largely the same between WT and *jaw-D* along the medial-lateral axis, with a slight increase in the medial quarter of *jaw-D*. This might be due to an expanded midrib. (D) Lobeyness is represented as a heatmap on sample WT 9 DAS leaf. (E) Stomatal spacing is represented as a heatmap on sample WT 9 DAS leaf. Black scale bars = 200 µm. Use of density plots, coloring, axis selection and normalization as in Figure 4.

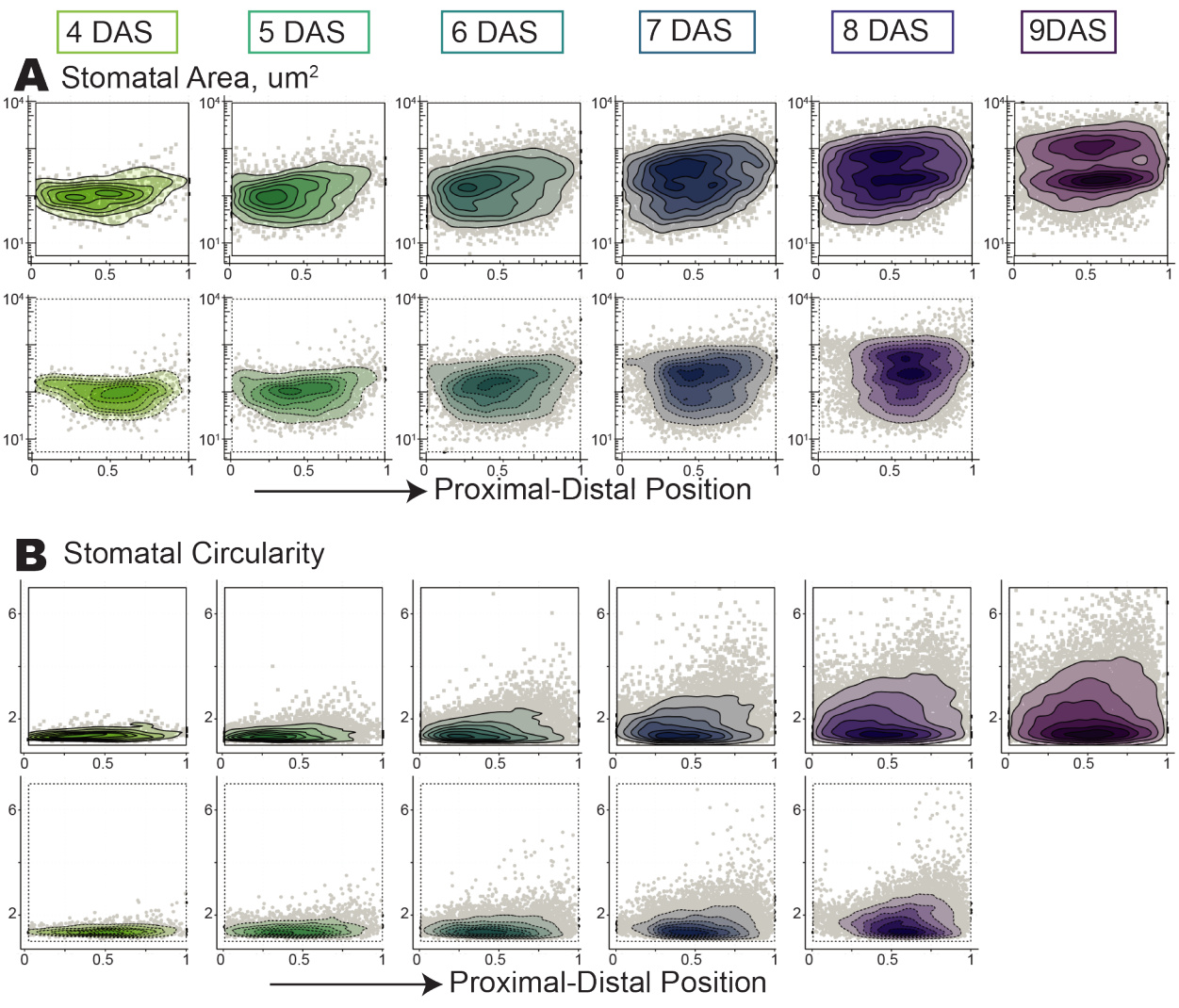

Supplemental Figure 8. | Additional stomatal differentiation quantification

(A-B) Area (A) or circularity (B) (perimeter/4pi*r^2) versus position along the proximal-distal axis for each stomate in all three WT (top, squares, solid lines) or *jaw-D* (bottom, circles, dotted lines) lamina replicates. (A) Stomatal area shows a distal maxima with a graded decrease towards the base for WT samples starting at 5 DAS. Stomata in *jaw-D* have more even sizes. Note, as the stomatal areas cover many orders of magnitude over time, a log scale is used. (D) Stomatal circularity is further from 1 in WT in a graded pattern signifying anisotropic expansion from tip to base. *jaw-D* stomata are rounder throughout the lamina. These differences demonstrate how stomata may be subject to tissue-level anisotropy and maturation processes only in WT while baseline initiation and differentiation for their physiological role is maintained in WT and *jaw-D*. Use of density plots, coloring, axis selection and normalization as in Figure 4.

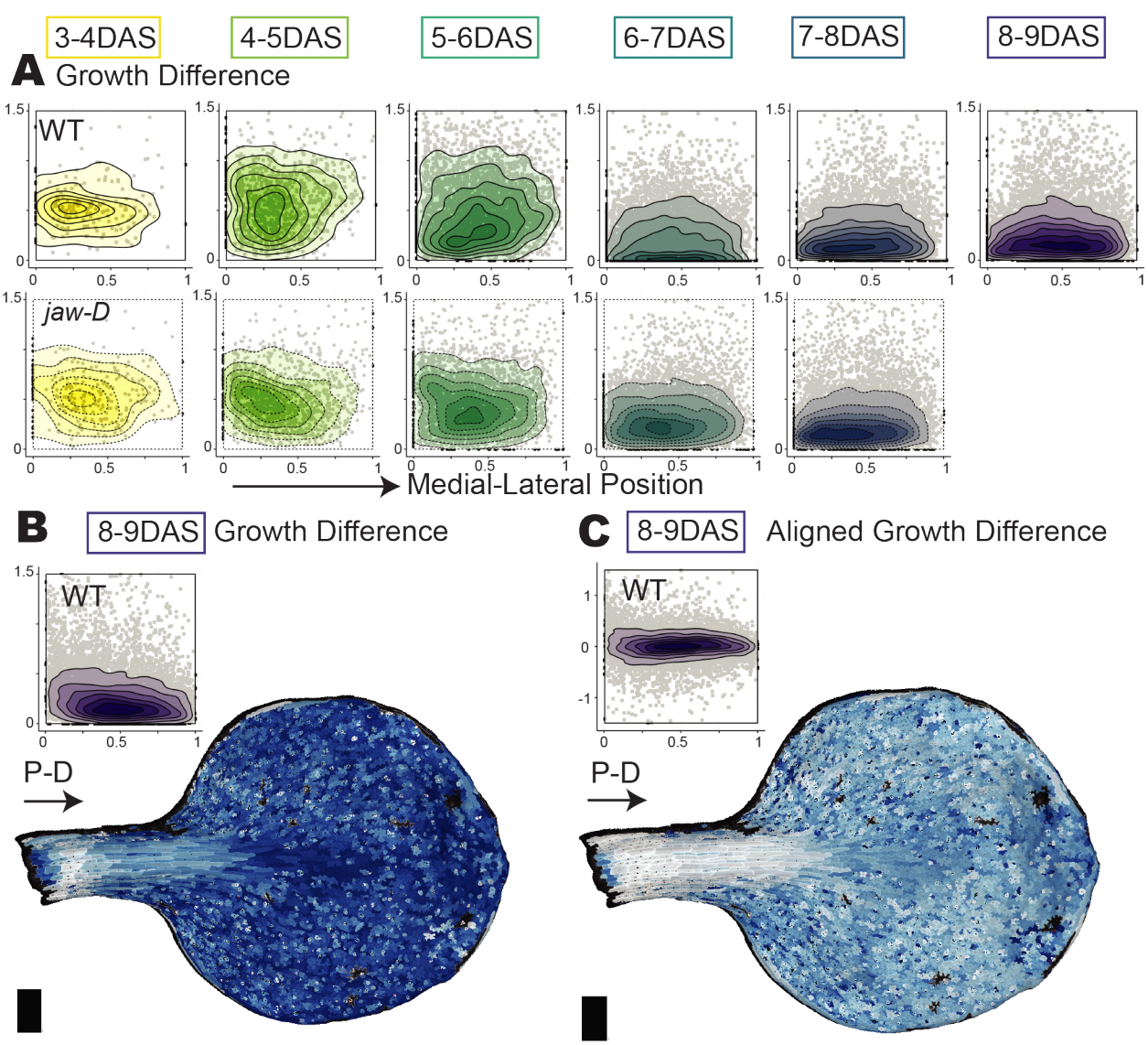

Supplemental Figure 9. | Additional growth orientation analysis

(A) Growth difference versus position along the medial-lateral axis for each cell in all three WT (top, squares, solid lines) or *jaw-D* (bottom, circles, dotted lines) lamina replicates. WT growth anisotropy varies more along the medial-lateral axis at 4-5 DAS and 5-6 DAS than *jaw-D;* otherwise anisotropy generally shows an even spread between 0 and 0.5. (B-C) Growth difference (B) and growth difference along the proximal-distal axis (C) as in main Figure 7 for WT at 8-9 DAS in lamina. Black scale bars = 200 µm. Use of density plots, coloring, axis selection and normalization as in Figure 4.

Supplemental Figure 10. | Higher resolution image of main text 8 DAS WT leaf (right) and its corresponding, to scale, 3 DAS primordia (left). Black bar = 200 µm.

Supplemental Figure 11. | Higher resolution image of main text 8 DAS *jaw-D* leaf (right) and its corresponding, to scale, 3 DAS primordia (left). Black bar = 200 µm.

Supplemental Figure 12. | Higher resolution image of replicate 8 DAS *jaw-D* leaf (right) with less visual skew and its corresponding, to scale, 3 DAS primordia (left). Black bar = 200 µm.

Supplemental Figure 13. | Higher resolution image of replicate 8 DAS *jaw-D* leaf (right) and its corresponding, to scale, 3 DAS primordia (left). Black bar = 200 µm.

Supplemental Figure 14. | Higher resolution image of replicate 8 DAS WT leaf (right) and its corresponding, to scale, 3 DAS primordia (left). Black bar = 200 µm.

Supplemental Figure 15. | Higher resolution image of replicate 8 DAS WT leaf (right) and its corresponding, to scale, 3 DAS primordia (left). Black bar = 200 µm.

Video 1. | Curvature cross-sections of WT and *jaw-D* 2.5D mesh representations of WT (left, top) and *jaw-D* (right, bottom) 8 DAS samples arranged in MorphoGraphX software. Meshes overlaid to compare curvature at comparable cross-section locations. Clipping plane (white lines) used to scroll through mesh sections to show proximal curvature increase in *jaw-D*. White scale bar = 200 um

Video 2. | 4-8 DAS clonal lineage with animated growth in WT Clonal lineages traced from 4 DAS to 8 DAS on example WT mesh. Individual lineages indicated as different label colors. Unlabeled cells could not be traced between all time points. Proximal lineages tend to divide and expand many times and often anisotropically, while distal lineages are more isotropic, expand and divide less. Black scale bar = 200 um

Video 3. | 4-8 DAS clonal lineage with animated growth in *jaw-D* Clonal lineages for a *jaw-D* sample with representation as in Video 2. All lineages are generally more isotropic in expansion and divide less.

Video 4. | Clonal lineage of 4 DAS and 8 DAS WT meshes in MGX Mesh representations of 4 DAS (right) and 8 DAS (left) meshes of sample WT leaf in MorphoGraphX software. Video begins showing 4 DAS sample with segmented cells indicated with different colored labels. Zoom out shows relative sizes and morphology changes from 4 DAS to 8 DAS. Parent labels are then displayed on 8 DAS mesh to indicate how cells labeled in 4 DAS mesh contributed to 8 DAS sample. Relatively simple, isotropic cells in an amorphous nub have become lobed pavement cells and stomata while the gross leaf morphology has changed to a distinct petiole and flattened, round blade. Black scale bar = 200 um.

Video 5. | Clonal lineage of 4 DAS and 8 DAS *jaw-D* meshes in MGX Representations as in Video 4 for *jaw-D* 4 DAS (left) and 8 DAS (right) sample meshes. 8 DAS mesh in *jaw-D* exhibits enhanced proximal curvature, and smaller, less lobed cells. Clonal patches are also smaller. Black scale bar = 200 um.

Video 6. | FEM simulations of leaf mesh growth as in main text Figure 9C. Color indicates growth ratio. Phase 1 with anisotropic growth throughout the leaf.

Video 7. | FEM simulations of leaf mesh growth as in main text Figure 9D. Color indicates growth ratio. WT-like phase 2 with anisotropy fanning out from the base of the leaf. This anisotropy pattern permits flattening.

Video 8. | FEM simulations of leaf mesh growth as in main text Figure 9E. Color indicates growth ratio. *Jaw-D*-like phase 2 with anisotropy high near the midrib across the length of the leaf. This anisotropy pattern induces curvature.

Supplemental Methods

Cellular Fourier transform

Here we define the discrete Laplace operator, we explain how we built the Fourier harmonics based on this Laplace operator, we define cell growth and deformation, and detail how we performed the spectral analysis based on CFTs. The theoretical basis of the CFT may be found in [1].

I. DISCRETE LAPLACE OPERATOR

To compute the Laplace operator, we consider the cells' minimal surfaces whose contours are the cells' contours. For each cell, we project its contour on a plane that is perpendicular to its surface vector. The contour being polygonal, the surface vector can be written $1/2\sum_n \vec{r}_n \wedge \vec{r}_{n+1}$ where the sum is over the contour vertexes, $\vec{r}_n$ is their position, n indexes the position around the contour and $\wedge$ is the exterior product. We then triangulate the surface enclosed in the projected contour using the MESH2D Matlab package [2, 3]. To obtain a mesh approximating the 3D minimal surface, we then interpolated positions in the mesh along the surface vector in using cell contours. The area $S_{i,t}$ for cell i at time t is then computed as the sum of areas of triangles in the triangulation, $S_{i,t} = \sum_m^{(i,t)} dS_m$, where m spans triangles of cell i at time t and dS_m is the area of triangle $\#m$. The tissue is made of N cells that are followed from t to $t+1$.

The discrete Laplace operator is a square matrix of size $N \times N$ and its components are given by

$$\bar{L}_{ij,t} = \delta_{ij} - \bar{W}_{ij,t}, \text{ with, } \bar{W}_{ij,t} = \sqrt{\frac{S_{i,t}}{S_{j,t}}} \frac{\sum_m^{(i,t)} dS_m \sum_n^{(j,t)} dS_n \exp(-d_{mn}/(5\,\ell_c))}{\sum_m^{(i,t)} dS_m \sum_j \sum_n^{(j,t)} dS_n \exp(-d_{mn}/(5\,\ell_c))}, \tag{1}$$

where indices $i = 0, 1, ..N-1$ and $j = 0, 1, ..N-1$ span the N cells of the tissue. d_{mn} is the distance between triangle m from cell i and triangle n from cell j, both considered at time step t. The unit of length is mean cell size $\ell_c = \sqrt{S_t/N}$, where S_t is the surface of the tissue at time t and N is the number of cells. Here we took the width $5l_c$ for the coarse Laplace operator.

II. FOURIER HARMONICS

We start from the singular value decomposition of the Laplace operator $\bar{L}$, which yields left singular vectors V, right singular vectors U, and the singular values $\hat{L}_k$:

$$\bar{L}_{ij,t} = \sum_{k=0}^{N-1} \hat{L}_k\, V_{ki} U_{kj}. \tag{2}$$

The value taken by the kth-harmonic in cell i at time step t is $1/S_{i,t}U_{ki}$. The spatial frequency of the kth harmonic is given by $f_k = 1/(5\pi)\, Q(\hat{L}_k)$, with $Q(l) = \sqrt{(1-l)^{-2/3} - 1}$. The harmonics are indexed so that their index grows with the wave number.

III. CELL DEFORMATIONS & GROWTH

To define the deformation of a cell i, we look for the linear transformation which best deforms the cell's contour at time t into it's contour at time $t+1$ (the contour of daughter cells if the cell i divides from t to $t+1$). Both cell contours are first projected perpendicularly to their surface vectors. The coordinates $\vec{r}_{n,t}$ and $\vec{r}_{n,t+1}$ of their vertexes are considered in two orthogonal basis of their projection planes, centered at the cell center. The best deformation is obtained in finding the matrix M_i which minimizes a cost function $d(M_{i,t} \cdot \vec{r}_{n,t}, \vec{r}_{n,t+1})$. The cost function d is build from the the euclidean distance $|.|$ and has for expression,

$$d(\vec{r}_{n,t}, \vec{r}_{n,t+1}) = \sum_j^{(i)} \sum_{n \in \mathcal{V}_{j,t}} \text{Min}_{n' \in \tilde{\mathcal{V}}_{j,t+1}} |\vec{r}_{n,t} - \vec{r}_{n',t+1}|^2 + \sum_j^{(i)} \sum_{n' \in \tilde{\mathcal{V}}_{j,t+1}} \text{Min}_{n \in \mathcal{V}_{j,t}} |\vec{r}_{n,t} - \vec{r}_{n',t+1}|^2,$$

where the sum $\sum_j^{(i)}$ is over the neighboring cells, $\mathcal{V}_{j,t}$ are the vertex of the cell's contour also neighbor with j at t, and $\tilde{\mathcal{V}}_{j,t+1}$ is the vertex to the corresponding segment of the cell contour at time $t+1$. A polar decomposition can be made of the matrix $M_{i,t} = R_{i,t} \cdot D_{i,t}$, where R is an arbitrary rotation and $D_{i,t}$ gives the cell deformation in the reference frame of the cell contour at time t. If this matrix describes well the cell's deformation, its eigenvectors give the principal and secondary direction of growth, the relative difference between the first and the second eigenvalue $d_{i,t}^{(1)}$ and $d_{i,t}^{(2)}$ gives an estimate for the cell growth anisotropy while their product should be $1 + G_{i,t}\Delta t$ with $G_{i,t}$ the areal growth rate and Δt, the delay between two time steps. The cell's areal growth rate $G_{i,t} = (\tilde{S}_{i,t+1}/S_{i,t} - 1)/\Delta t$ can also be calculated from its surface area $S_{i,t}$ at time t, and $\tilde{S}_{i,t+1}$ at time $t+1$ (if the cell i divides from t to $t+1$, $\tilde{S}_{i,t+1}$ is the surface area of the daughter cells). We found a good agreement between this last expression of $G_{i,t}$ and $d_{i,t}^{(1)} d_{i,t}^{(2)}$. The matrices $D_{i,t}$ being defined in bases of each cells' tangent planes, we then consider $D_{i,t}^{(3D)}$ the deformation matrices in a unique basis of the 3D space, the deformation along the surface vector being taken equal to zero.

IV. SPECTRAL ANALYSIS

We applied our spectral analysis to the areal growth rate and the deformation. For the areal growth rate we used the formula $G_{i,t} = (\tilde{S}_{i,t+1}/S_{i,t} - 1)/\Delta t$. The kth CFT coefficient for the areal growth rate is then $\hat{G}_{k,t} = \sum_i U_{ki} G_{i,t} \sqrt{S_{i,t}/S_t}$ where S_t is the total area $S_t = \sum_i S_{i,t}$. Here we use a convention that differs from [1] by a multiplicative factor $1/\sqrt{S_t}$ in the definition of the CFT. This makes the interpretation of CFTs simpler: they have the same dimensions (units) as the original signal (here growth) and the first coefficient is equal to the average signal. For the deformation matrix in 3D $D_{i,t}^{(3D)}$, we computed the CFT, $\hat{D}_{k,t} = \sum_i U_{ki} D_{i,t}^{(3D)} \sqrt{S_{i,t}/S_t}$.

Spectra are obtained in representing CFTs as functions of the space frequency of the harmonics they are associated to. In the case of deformation, representing the spectra is made complicated by the high number of the matrix's components, and another difficulty is to compare the spectra of different tissues whose orientations are arbitrary. To analyze the deviation of growth from isotropy we can nevertheless consider the difference $\hat{d}_{k,t}^{(1)} - \hat{d}_{k,t}^{(2)}$ between the two higher eigenvalues of $\hat{D}_{k,t}$, $\hat{d}_{k,t}^{(1)}$ and $\hat{d}_{k,t}^{(2)}$ which we represent once again as functions of the spatial frequency of the harmonics they are associated to. To compare different tissues and genotypes, and since Fourier harmonics are specific to each tissue, we smooth spectra to obtain an estimate of spectral densities. The smoothing is made for every tissue with a Gaussian kernel of width 0.16 and is relative to the spatial frequency f_k. We also merge the spectra of identical stage and genotype. We estimate the standard error assuming the CFTs to be statistically independent and to be well described by distributions varying smoothly with respect to the spatial frequency.

[1] Antoine Fruleux and Arezki Boudaoud. Cellular fourier analysis for geometrically disordered materials. *Physical Review Research*, 3(2):023036, 2021.

[2] D Engwirda. Unstructured mesh methods for the navier-stokes equations. *Undergraduate Thesis, School of Engineering, University of Sidney*, 2005.

[3] Darren Engwirda. Locally optimal delaunay-refinement and optimisation-based mesh generation. 2014.